# Stochastic Modeling of Calcium in 3D Geometry

Tomáš Mazel,[†] Rebecca Raymond,[†] Mary Raymond-Stintz,[†] Stephen Jett,[‡] and Bridget S. Wilson[†*]
[†]Department of Pathology and Cancer Research and Treatment Center, and [‡]Department of Cell Biology and Physiology, University of New Mexico School of Medicine, Albuquerque, New Mexico

ABSTRACT Release of inflammatory mediators by mast cells in type 1 immediate-hypersensitivity allergic reactions relies on antigen-dependent increases in cytosolic calcium. Here, we used a series of electron microscopy images to build a 3D reconstruction representing a slice through a rat tumor mast cell, which then served as a basis for stochastic modeling of inositol-trisphosphate-mediated calcium responses. The stochastic approach was verified by reaction-diffusion modeling within the same geometry. Local proximity of the endoplasmic reticulum to either the plasma membrane or mitochondria is predicted to differentially impact local inositol trisphosphate receptor transport. The explicit consideration of organelle spatial relationships represents an important step toward building a comprehensive, realistic model of cellular calcium dynamics.

## INTRODUCTION

Activation of mast cell IgE receptors (Fc$\varepsilon$RI) by allergens is the underlying mechanism of type I hypersensitivity reactions (1). Secretion of histamine and other preformed inflammatory mediators is dependent on the increase of intracellular calcium, mediated by release from the intracellular endoplasmic reticulum (ER) stores and the secondary influx of extracellular calcium (2). Signaling is initiated by antigen-induced IgE receptor aggregation, followed by Lyn-mediated phosphorylation of immunoreceptor tyrosine-based activation motifs and recruitment of the tyrosine kinase Syk (3). Phospholipase C$\gamma$ (PLC$\gamma$), an important downstream target of the Fc$\varepsilon$RI signaling cascade, is upregulated by both tyrosine phosphorylation and allosteric activation by products of PI 3-kinase (4). PLC$\gamma$ catalyzes the hydrolysis of phosphatidylinositol(4,5)$P_2$, producing diacylglycerol and inositol trisphosphate ($IP_3$). $IP_3$, in turn, activates $IP_3$R calcium channels localized in the ER membrane, thus causing release of calcium from the ER store and increase in cytosolic calcium concentration. The decrease in the ER luminal calcium concentration is then sensed, with an important contribution from the STIM family of proteins (5), and signaled to plasma membrane store-operated calcium (SOC) entry channels (6), which mediate the influx of extracellular calcium. Orai1 proteins have recently emerged as candidates for the SOC channels (7). A number of mechanisms limit the duration of the calcium signal, including 1), ER and cytosolic buffering proteins; 2), calcium pumps and exchangers at the plasma and ER membranes; and 3), buffering by mitochondria.

The complexity of calcium signaling has provided a rich background for mathematical modeling (for review, see Schuster et al. (8)). Deterministic models have provided fundamental insights, many focused on specific details (9). Integration of calcium responses into the modeling of intracellular signaling networks is a more recent challenge. One such initiative is the Virtual Cell project, capable of placing receptor-initiated calcium signaling within a simplified cell geometry (10). Our own focus is aimed at a finer scale of spatial organization, based upon the hypothesis that the heterogeneity in cell structure and organization among individual cell types may have significant impact on intracellular calcium handling. We also consider calcium handling to be ideally suited to stochastic modeling, since there are relatively few (tens of thousands) calcium ions in the cytoplasm of resting cells.

Although the ER forms one continuous intracellular membrane network (11), it harbors many specialized domains. The three classical ER compartments (nuclear envelope, and rough and smooth ER) are easily recognizable. In addition, the ER includes special areas of close contact with intracellular organelles that differ in their composition from the rest of the ER (12). These so-called membrane contact sites (MCS) have been implicated in the trafficking of lipids, phagocytosis and calcium signaling (13).

In a previous study (14), we used a hybrid reaction-diffusion model to evalute calcium release from clustered and unclustered $IP_3$ receptors ($IP_3$Rs). A meshed 3D reconstruction of the ER was used as the underlying geometry, with opening of the $IP_3$R as the sole stochastic element. Here we extend this study by considering the ER's proximity to both the plasma membrane and mitochondria. Our aim was to develop computationally frugal methods to evaluate the importance of considering complex intracellular geometry in models of cell signaling. First, we determine how diffusion of particles within compartments is limited by the geometry of organellar membranes. Next, we present a fully stochastic model of $IP_3$-mediated calcium release. The stochastic model includes key early steps in the process, including $IP_3$ synthesis and degradation, diffusion away from the source, and reaction with $IP_3$ receptors. Calcium uptake by individual mitochondria is explicitly considered, in preference to the usual treatment of mitochondria as

*Submitted April 15, 2008, and accepted for publication October 15, 2008.*

*Correspondence: bwilson@salud.unm.edu

Editor: Ian Parker.



0006-3495/09/03/1691/16 $2.00

doi: 10.1016/j.bpj.2008.10.066

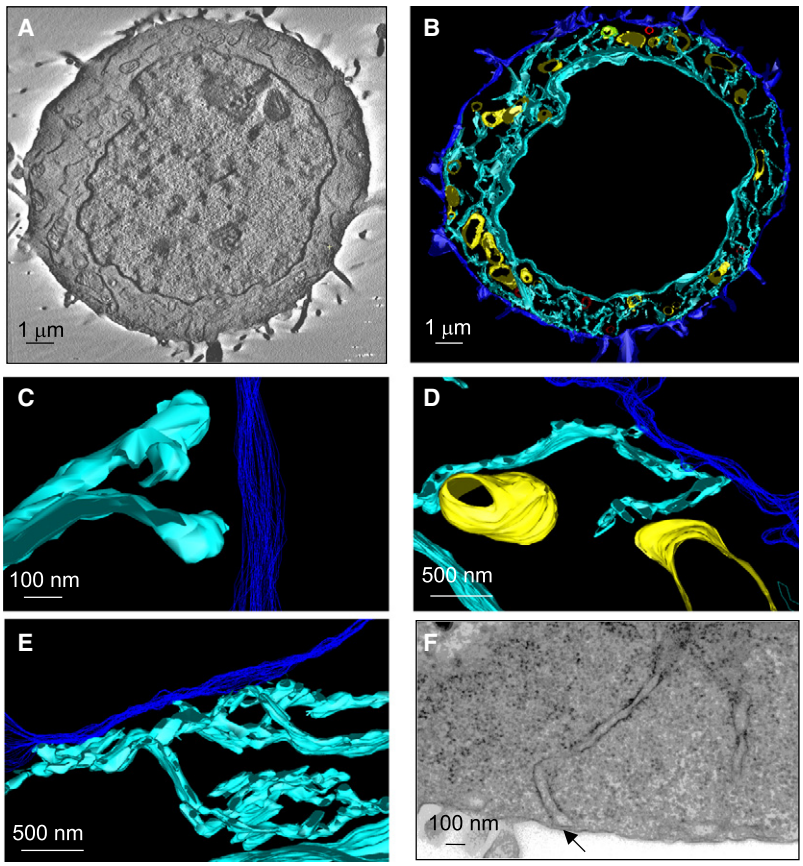


FIGURE 1 RBL-2H3 3D reconstruction. (*A*) Tilt series of electron microscopy images. (*B*) 3D reconstruction. (*C–F*) Details showing portions of the endoplasmic reticulum closely approaching the plasma membrane (*C* and *E*) and mitochondria (*D*). (*F*) ER-plasma membrane contact sites. Note the transition from the rough to smooth character of the ER as it comes closer to the plasma membrane (*arrow*).

a simple immobile buffer. Results in the stochastic model are confirmed by partial-differential-equation (PDE)-based reaction-diffusion simulations within the same cellular geometry. PDE simulations were also used to efficiently evaluate the effect that nearby organelles have on $IP_3R$-mediated release.

## MATERIALS AND METHODS

### Tomography and organelle reconstruction

Rat basophilic leukemia (RBL-2H3) cells were cultured on tissue culture grade plastic in minimal essential medium (Gibco, Gathersburg, MD) supplemented with 15% fetal calf serum (HyClone, Logan, UT), penicillin-streptomycin and L-glutamine. Cells were fixed with 2% glutaraldehyde in 0.1 M sodium cacodylate buffer, then lifted from plastic dishes by the addition of propylene oxide (15) and processed for Epon embedding as described by Pfeiffer et al. (16). Blocks were stained with uranyl acetate and cut as 1.0-$\mu$m sections with a Leica Ultracut S microtome. Sections were mounted on 75 mesh clamshell grids and further stained for 15 min with 2% uranyl acetate and 2 min with Sato lead solution, then carbon-coated. Before imaging, sections were dipped in 10 nm colloidal gold suspension (Sigma, St. Louis, MO) to provide markers for tilt series alignment. Samples were imaged in a 400EX (Jeol, Peabody, MA) intermediate high-voltage electron microscope (National Center for Microscopy and Imaging Research (NCMIR), University of California, San Diego). Before image capture, samples were exposed to the beam for 45 min to preshrink the specimen and prevent further deformation during the tilt series capture. Photographic images were captured at 0.6° and then digitized at 14 bits with a Photometrics CH250 CCD camera. Image alignment and back projection were performed with XFido software (NCMIR). Tracing, 3D reconstruction, and meshing were performed using the IMOD 3.5.3 program (University of Colorado Laboratory for 3D Electron Microscopy of Cells, Boulder, CO).

### Programming and computer analysis

Computer programming was performed in MATLAB (The Mathworks, Natick, MA). Simulations were performed using a personal computer or, when needed, on a cluster of Linux-based computers. The 3D reconstruction was converted into bitmaps with a voxel size of 28 × 28 × 3.33 nm (or detail size of 5 × 5 × 3.33 nm) and color coding for individual organelles. These images were then converted into an integer-value matrix that was used in further calculations. Detailed descriptions of algorithms and strategies for parameter estimation are given in the Appendix.

## RESULTS AND DISCUSSION

### 3D reconstruction of an RBL cell

A tomographic tilt series of electron microscopy images was taken from a 500-nm-thick section through the nuclear region of an RBL-2H3 cell stimulated with IgE plus antigen (1 $\mu$g/ml DNP-BSA) for 5 min (Fig. 1 *A*). Of these, a slab of 133 nm (~1.4% of the cell volume) was used for 3D reconstruction (Fig. 1 *B*). Table 1 shows the percent distribution of individual intracellular organelles in the reconstructed volume, as well as estimated values for the whole cell. Since the section crosses the nuclear region of the cell, nucleus overrepresentation has been considered.

**TABLE 1 Organelle volumes**

| Organelle | In reconstruction | Cell estimate | Volume ($\mu m^3$) in reconstruction | Volume in cell ($\mu m^3$) |
|---|---|---|---|---|
| Nucleus | 49.7% | 35.5% | 11.10 | 550 |
| Mitochondria | 3.6% | 4.6% | 0.80 | 71 |
| ER | 4.2% | 4.9% | 0.94 | 76 |
| Cytoplasm | 39.9% | 51.1% | 8.91 | 792 |

Details showing the spatial relationship between the ER (*aqua*), plasma membrane (*blue*), and mitochondria (*yellow*) are shown in Fig. 1, *C–E*. Note that there are several sites at which the ER is within a very short distance (<50 nm) of the plasma membrane. We estimate that in our 3D reconstruction there are ~30 such contact sites, corresponding to ~1.5% of the ER membrane area. Fig. 1 *F* provides a representative view of these ER-plasma membrane contact sites (''cortical ER''), as imaged by ultrathin sectioning and transmission electron microscopy. We noticed that sections of the ER near the plasma membrane tended to widen (Fig. 1 *C*), with a smooth appearance indicating lack of polysome attachment (Fig. 1 *F*). These observations are consistent with the concept that cortical ER is a specialized domain.

To describe the morphology more quantitatively, we measured the distances between individual organelles (Fig. 2, *A–C*). Whereas the ER came very close to both the plasma membrane and mitochondria, there were no contact sites observed between mitochondria and plasma membrane. The ER-plasma membrane distance histogram shows two peaks corresponding to cortical ER (at ~150 nm) and the nuclear envelope (at 1.1 $\mu$m). This is consistent with similar observations in many other cell types (11). Distances between ER and mitochondria peak at ~0.3 $\mu$m and between plasma membrane and mitochondria at ~0.6 $\mu$m. Fig. 2, *D–F*, shows the probability that a diffusible second messenger released from either plasma membrane (Fig. 2 *D*), endoplasmic reticulum (Fig. 2 *E*), or mitochondria (Fig. 2 *F*) will encounter the membrane of the other organelles at a given distance. To accomplish this, the cell volume was considered as a matrix, with voxel dimensions of 28 × 28 × 3.3 nm for whole cell modeling and of 5 × 5 × 3.3 nm for detailed local models. The probabilities shown represent the likelihood that a diffusible particle will fall into a voxel designated as plasma membrane, ER, or mitochondrial membrane, relative to the distance from the source.

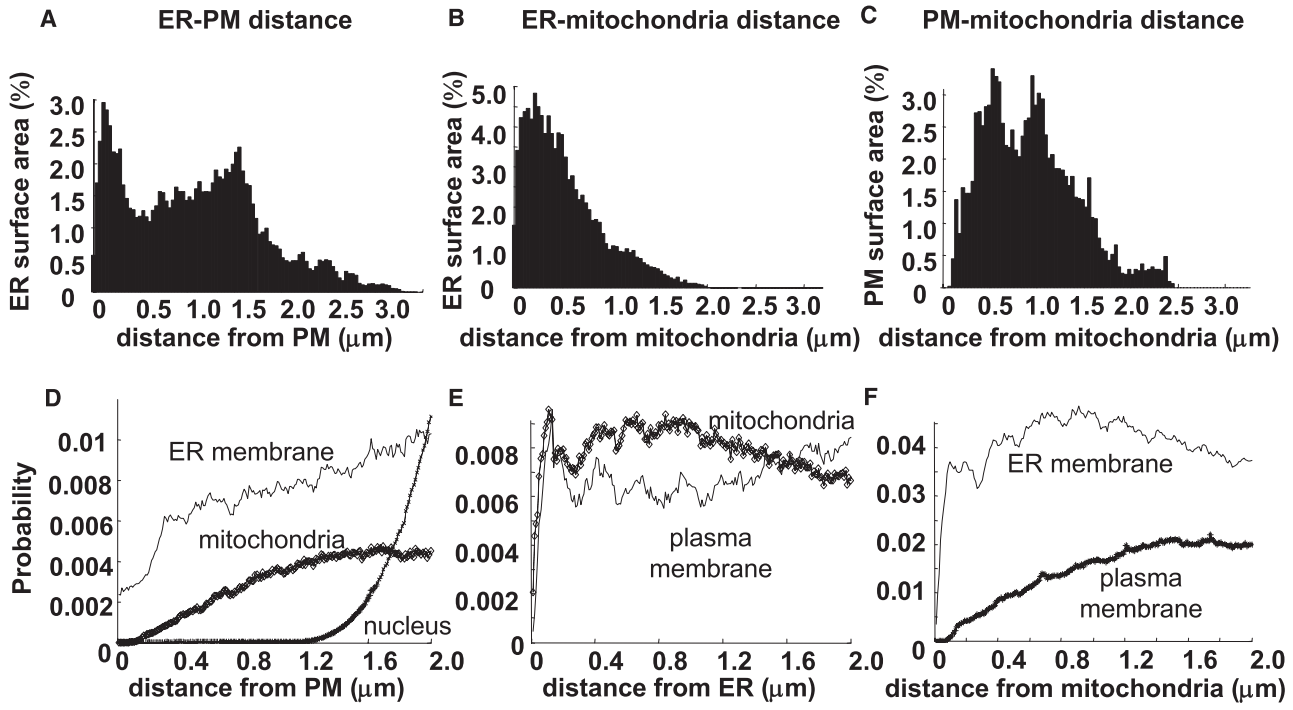


FIGURE 2 Distribution of interorganellar distances. (*A–C*) Histograms of distances between the ER and plasma membrane (*A*), ER and mitochondria (*B*), and plasma membrane and mitochondria (*C*). Note the presence of close contacts between the ER and the plasma membrane and the ER and mitochondria (*A* and *B*) and their absence between the plasma membrane and the mitochondria (*C*). Note also the two peaks in *A* corresponding to the cortical ER and the nuclear envelope. To calculate distances between organelles, we wrote a code that runs through all the voxels of a given cellular structure (e.g., the ER membrane *A*) and computes their distance from the closest voxel of another structure of interest. (*D–F*) Graphs showing the probability of encountering certain organelles at a certain distance in the cases where the signal starts at the plasma membrane (*D*), the ER (*E*), and the mitochondria (*F*). Again, the close contacts between the ER and plasma membrane (*D* and *E*) and the ER and mitochondria are clearly visible. The code used to obtain these plots ran through all the voxels of a given structure (e.g., the plasma membrane in *D*). There were 20,000 points positioned on 200 concentric spheres with radii ranging from 1 to 200 nm, each containing 100 evenly distributed points. The center of these spheres was set into the center of the particular voxel's surface, facing the cytosol. Each of these 20,000 points was then checked and assigned to a particular structure, depending on the value of the voxel they fell into.

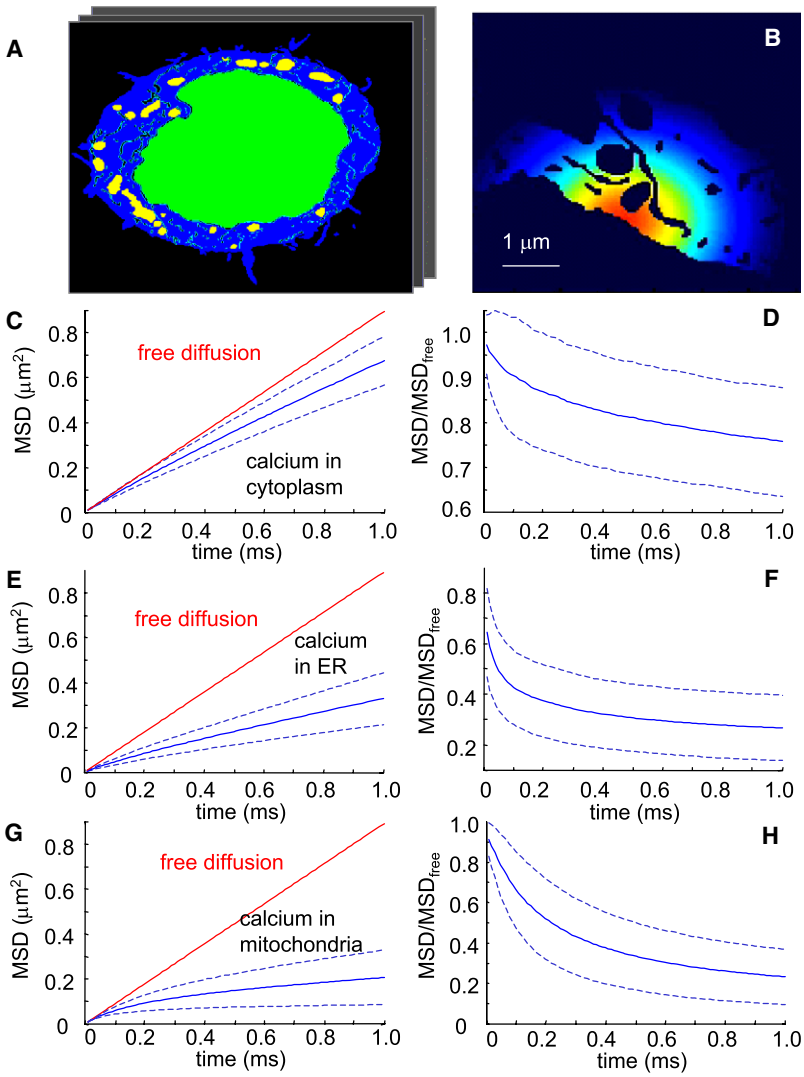


FIGURE 3 Intracellular geometry limits diffusion of substances compared to free solution. (*A*) Color coding of individual intracellular compartments: *blue*, cytosol; *yellow*, mitochondria; *green*, nucleus; *gray*, ER membrane. The resulting mask matrix formed the basis of most of the models presented. (*B*) One million test particles were placed at a point in the plasma membrane and allowed to diffuse in the cytosol, and their mean-squared displacement was calculated. (*C–H*) Comparison between the time course of the mean-squared displacement (MSD) in free solution and in individual intracellular compartments (results show MSD in the *xy* plane). The diffusion coefficient for calcium (223 $\mu m^2/s$) was used as an example. The particles in this simulation did not react, bind, or cross the boundaries between the compartments. *Solid lines*, mean; *dashed lines*, $\pm$SD.

## Intracellular geometry limits diffusion

Fig. 3 demonstrates how cellular geometry influences the diffusion of particles within compartments, plotted as mean-square displacement (MSD). Fig. 3 *A* shows the 3D matrix used as a mask to define compartments. A stack of these masks was assembled, using up to 80 thin slices to create the 3D volume. Fig. 3 *B* illustrates a wave of particles ($10^6$) stochastically released in silico from the plasma membrane. These simulations were repeated at many sites, and MSD values within each compartment were compared to a theoretical value for free diffusion (Fig. 3, *C–H*). Results show that diffusion is only slightly restricted in the cytoplasm (~85% of the theoretical value). In contrast, particles diffusing within the restricted spaces of the ER and mitochondria are considerably restricted (MDS 25–30% of the theoretical value). For simplicity, we chose diffusion coefficients corresponding to calcium ions (unbuffered and nonreacting).

## Fully stochastic simulations of $IP_3$ production, diffusion, and channel activation

Stochastic approaches are appropriate when concentrations are low. This is the case for cytosolic calcium ions, particularly in unstimulated cells where the resting concentration of free calcium is ~100 nM. Fig. 4 illustrates this concept by showing that the number of calcium ions present in the cytoplasm of a thin cell slice (~$2 \times 2 \times 0.2$ $\mu$m) is <20. This figure also illustrates how cell geometry is incorporated into a fully stochastic approach to track calcium diffusion, reaction, and transport processes. As in Fig. 3, an organelle ''mask'' was based upon the original electron microscope image shown here. Buffers and transport proteins were assigned to each organelle membrane or its aqueous compartment.

Orange spots in Fig. 4 *A* show the approximate location of diffusing free calcium ions, represented by a Gaussian point-spread function around its original location and a time step of

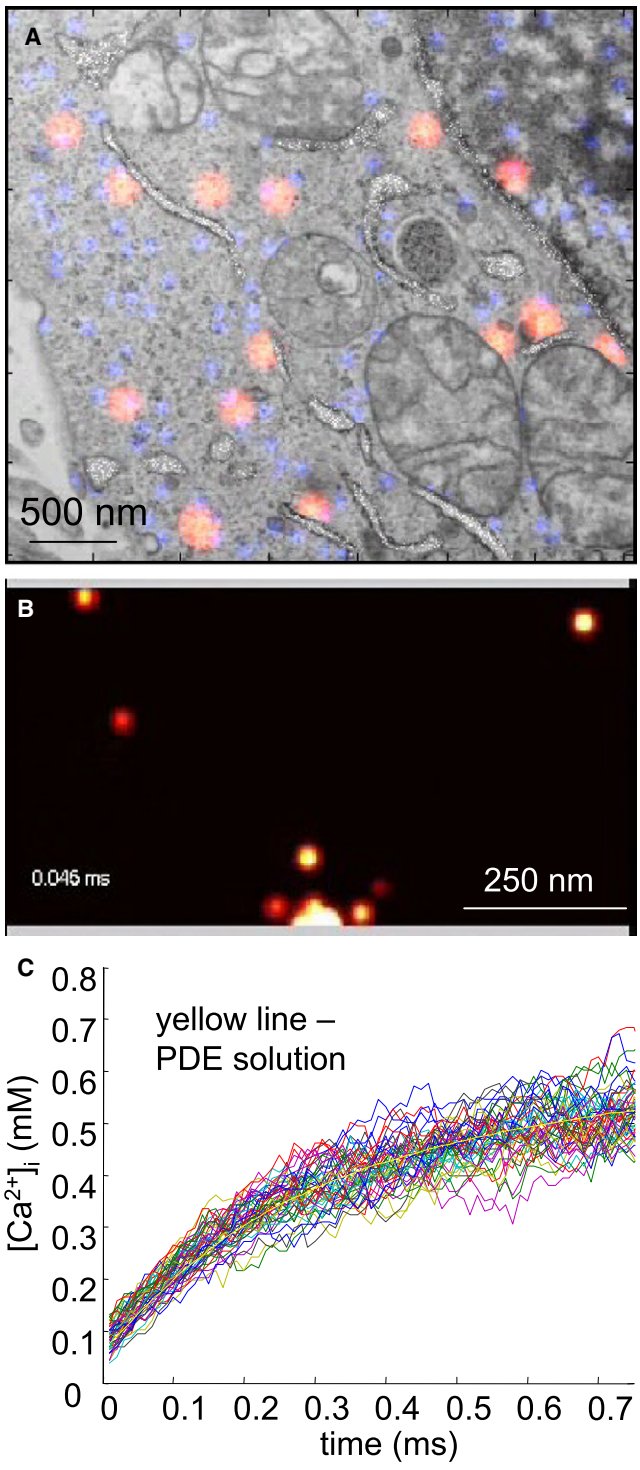


FIGURE 4 Use of EM images to define 3D environment for stochastic modeling of calcium signaling. (*A*) Orange and blue spots show the random cytoplasmic distributions of calcium ions and calmodulin molecules, respectively, when superimposed upon the electron microscopy image used to define cell geometry in the stochastic simulation space. Other components of the model (transporters, calreticulin) are not shown for simplicity's sake. Slice thickness, 0.2 $\mu$m. This figure is a snapshot of Movie S2. (*B*) 3D box geometry illustrating stochastic release of calcium ions from a single $IP_3R$ located on one box side. (*C*) PDE solutions compared with stochastic solutions for $[Ca^{2+}]_i$ averaged over a hemisphere centered at the channel mouth (radius 500 nm). The smooth yellow line represents the PDE solution, whereas other colored lines show the variability among many stochastic simulations.

10 $\mu$s. Blue spots represent diffusing calmodulin molecules. A movie illustrating the diffusive behavior of both calcium and calmodulin, as well as calcium transport dynamics, is provided (see Movie S1 in the Supporting Material). In the movie, calcium spots occasionally disappear as they bind to buffer proteins or enter organelles. The model was designed in MatLab (see Appendix) and is easily adaptable to new geometries based on electron micrographs. It should also be applicable to 3D reconstructions acquired by confocal imaging, which would permit capture of dynamic details of organelle movements and shape changes.

In Fig. 5, we apply the stochastic model to a relatively simple problem: the release of $IP_3$ at the plasma membrane, its degradation and binding, and activation of the $IP_3Rs$ at the ER membrane. Parameters for $IP_3$ production and metabolism are shown in Table 2, and the simulation space is increased to a 3D thickness of 266 nm by adding additional layers of the original geometry. In brief, PLC$\gamma$ molecules were placed at random locations at the plasma membrane, at a density estimated from immunogold labeling values reported for activated RBL cells in Wilson et al. (17) and either 100% or 10% of the total PLC$\gamma$ was activated at time $t = 0$, a strategy that generated antigen-stimulated $IP_3$ production rates similar to measurements reported in Smith et al. (18).

RBL cells express only ~14,000 tetrameric $IP_3Rs$ (19), each with a capacity for high conductance. Most of the $IP_3Rs$ in RBL-2H3 cells are type II (70%), with only 10% type I and 20% type III receptors (19). Depending on the state of the cell, these $IP_3Rs$ can be either homogeneously distributed in the ER or grouped together in clusters of 100–200 channels (14,19,20). For these simulations, random or clustered channels were mapped on the ER geometry. For $IP_3R$ type II transport, we modified the eight-state DeYoung-Keizer model (21) to include a ninth state that results in more realistic open and closed times and reflects the fast channel kinetics (Fig. S1). The kinetic parameters were constrained to reflect the properties of $IP_3R$ type II receptors (22). This strategy is similar to the model described recently by Shuai et al. (23). We tested the application of the stochastic approach by comparing it to PDE solutions, using a simple 3D box geometry (Fig. 4 *B* and Movie S2). As shown in Fig. 4 *C*, the results from PDE and stochastic approaches are in good agreement.

Results shown in Fig. 5 *A* compare the total number of $IP_3s$ bound to $IP_3R$ (*left*), as well as the total number of active $IP_3Rs$ (four $IP_3s$ bound per tetramer), in response to activation of either 10% or 100% of the PLC$\gamma$ membrane fraction. We also evaluated whether clustering of the $IP_3R$ had a significant impact on the binding of $IP_3$ diffusing through the 3D simulation space. The impact of clustering, seen as

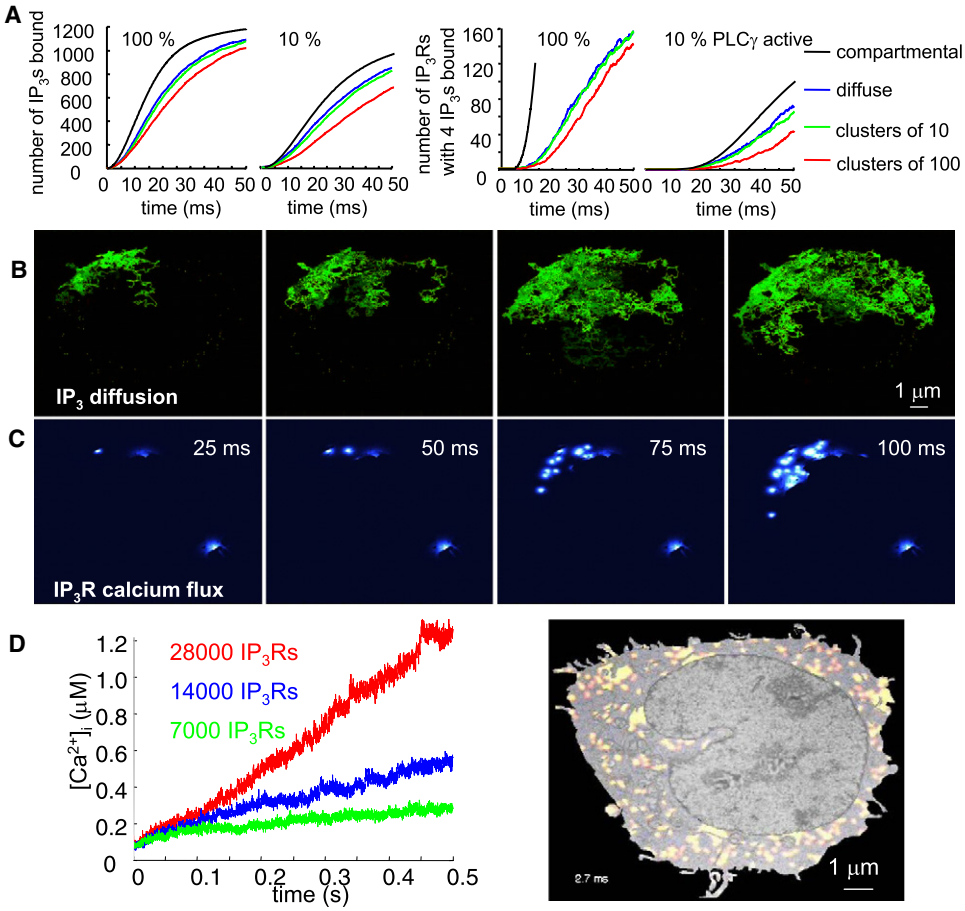


FIGURE 5 Simulation of $IP_3$ release, diffusion, and channel activation in a 3D stochastic model. (*A*) Comparison of compartmental and stochastic modeling of $IP_3$ release from the plasma membrane and its binding to $IP_3Rs$ in the ER. The stochastic simulation was based upon a fractional 3D cellular geometry with a depth of 266 nm. (*B*) $IP_3$ molecules released by phospholipase C diffuse from the plasma membrane and bind to the $IP_3Rs$ in the ER (see also Movie S4). (*C*) When all four $IP_3R$ subunits are in the activated state (i.e., with bound $IP_3$ and calcium at their activation site and no calcium at the inhibitory site), the channels open and release calcium. (*D*) Results of varying the number of $IP_3Rs$ from 7000 to 28,000. This simulation was based upon a more complete cellular geometry (image at right) and a depth of 100 nm.

slower activation due to local depletion of $IP_3$, is small but reproducible. For comparison, results using a compartmental modeling approach are shown as a solid black line. The stochastic simulation results, which are likely to be a more accurate estimation of the process, predict slightly slower binding kinetics.

Fig. 5 *B* illustrates the diffusion of $IP_3$, synthesized by PLCγ located in the upper left quadrant of the plasma membrane of the cell represented in the model (see Movie S3). The time course for binding of individual $IP_3$ molecules to clustered $IP_3Rs$ is represented by the series of images in Fig. 5 *C*. In addition to diffusion, individual $IP_3$ molecules in the simulation were subject to degradation at rates similar to those found by Smith et al. (18). As expected, $IP_3R$ clusters located close to the source of $IP_3$ production were activated preferentially (Fig. 5 *C*).

Fig. 5 *D* and Movie S4 show another application of this approach. We compared the effect of lowering the number of $IP_3Rs$ from 14,000/cell (as measured experimentally) to 7000 tetrameric channels or raising the levels to 28,000 channels/cell. As expected, the number of $IP_3Rs$ influences both the delay and the slope of cytosolic calcium concentration increase. The geometry (TEM image of an RBL cell) used for this simulation is shown in Fig. 5 *D* (thickness 100 nm).

## Simulations predict that mitochondria nearest to clustered $IP_3Rs$ respond quickly to take up calcium

Although it has long been recognized that mitochondria have a significant buffering capacity for calcium, most mathematical models of calcium dynamics do not consider them explicitly. In the geometric reconstruction, mitochondria are revealed as discrete organelles that are often surrounded by the ER membrane (Fig. 6 *A*). In Fig. 6, *C* and *D*, we use the spatial stochastic model to explicitly consider the proximity of individual mitochondria to clustered $IP_3$ receptors in the ER (see Movie S5 for a sample simulation). For comparison, results of PDE-based simulations within the same geometry are also shown (Fig. 6, *B* and *D*, and Movie S6). A full description of our simplified mitochondrial model is provided in the Appendix; it is based upon the work of Magnus and Keizer (24) and incorporates a representation of the mitochondrial uniporter activity, as well as the extensive buffer capacity of the mitochondrial matrix.

Portions of five mitochondria are within the simulation space. Two clusters of type II $IP_3Rs$ were placed on discrete sites in the ER membrane. In both simulation approaches, five and three channels in two clusters were opened deterministically and free calcium concentrations in both the

**TABLE 2 Modeling parameters**

| Parameter | Symbol | Value | Source |
|---|---|---|---|
| ***Initial conditions*** | | | |
| Resting $[Ca^{2+}]$ in cytosol | $Ca_{cyt\_0}$ | 75 nM | Mean of (53–57) |
| Resting $[Ca^{2+}]$ in ER | $Ca_{er\_0}$ | 500 $\mu$M | (57) |
| Resting mitochondrial $[Ca^{2+}]$ | $Ca_{mit\_0}$ | 0.61 $\mu$M | (58) |
| ***Mobile buffers*** | | | |
| Calreticulin | $Tot_{Ber\_0}$ | 0.175 mM | This study (Western blotting) |
| Calmodulin | $Tot_{Bcyt\_0}$ | 21.9 $\mu$M | This study |
| Mitochondrial buffer | $Tot_{Bmit}$ | 5 mM | (35) |
| ER membrane potential | $V_{m,\ ER}$ | 0 mV | |
| Resting $IP_3$ | $IP_3$ | 20 nM | Balance (also similar to (59) and (60)) |
| ***Diffusion coefficients*** | | | |
| Calcium in cytosol | $D_{ca\_cyt}$ | 223 $\mu m^2/s$ | (61) |
| Calcium in ER lumen | $D_{ca\_er}$ | 223 $\mu m^2/s$ | Unknown, equalled to cytosol |
| Calcium in mitochondrial matrix | $D_{ca\_mm}$ | 223 $\mu m^2/s$ | Unknown, equalled to cytosol |
| Calmodulin in cytosol | $D_{Bcyt}$ | 0.25 $\mu m^2/s$ | (62) |
| Calreticulin in ER | $D_{Ber}$ | 1.3 $\mu m^2/s$ | (Snapp, E. L., personal communication) |
| Mitochondrial buffer | $D_{mit\_buf}$ | 8 $\mu m^2/s$ | (35) |
| $IP_3$ in cytosol | $D_{IP3}$ | 283 $\mu m^2/s$ | (61) |
| **FLUXES** | | | |
| ER leakage | $J_{er\_leak}$ | | |
| Shutoff threshold | $J_{er\_leak\_off}$ | | |
| Balances SERCA + $IP_3R$ flux under resting conditions | | 7% resting $[Ca^{2+}]_{er}$ | (43) |
| SERCA | | | |
| Number of SERCA pumps/cell | | 1,600,000 | (14) |
| SERCA2b/SERCA3 ratio | | 1:1 | (41) |
| SERCA2b $K_m$ | $K_{SERCA2b}$ | 0.27 $\mu$M | (42) |
| SERCA3 $K_m$ | $K_{SERCA3}$ | 1.1 $\mu$ M | (42) |
| SERCA2b turnover rate | $V_{SERCA2b}$ | 4 $s^{-1}$ | (42) |
| SERCA3 turnover rate | $V_{SERCA3}$ | 12 $s^{-1}$ | (42) |
| Hill coefficient | $H_{SERCA}$ | 2 | (42) |
| PMCA | | | |
| Maximum overall rate | $V_{PMCA}$ | 17.5 $\mu$M/s | ($[Ca^{2+}]_i$) fitted according to (49) |
| PMCA4b/PMCA1b ratio | $V_{PMCA4}/V_{PMCA1}$ | 0.22 | Estimate, based on (44) |
| $K_m$ for calcium (no CaM) | $K_{PMCA,Ca,1}$ | 7 $\mu$M | (46) |
| $K_m$ for calmodulin | $K_{PMCA,CaM,1}$ | 28 nM | (46) |
| Factor for CaM activation | $f_{V\_PMCA,CaM,1}$ | 2 | (46) |
| Factor for CaM activation | $i_{K\_PMCA,CaM,1}$ | 7/2 | (46) |
| $K_m$ for calcium (no CaM) | $K_{PMCA,Ca,4}$ | 1.06 $\mu$M | (45) |
| $K_m$ for calmodulin | $K_{PMCA,CaM,4}$ | 9.8 nM | (45) |
| Factor for CaM activation | $f_{V\_PMCA,CaM,4}$ | 1/0.24 | (45) |
| Factor for CaM activation | $f_{K\_PMCA,CaM,4}$ | 1.06/0.16 | (45) |
| (in saturating CaM concentration) | $K_{PMCA,Ca,4}$ | drops to 0.16 $\mu$M) | (45) |
| NCX | | | |
| Maximum rate | $V_{NCX}$ | 129 $\mu$M/s | Fitted according to (49) |
| | $K_{d\_Act}$ | 0.256 $\mu$M | (47) |
| Basal NCX/basal PMCA activity ratio | | 0.33 | (50) |
| $K_m$ for extracellular sodium | $K_{Na,out}$ | 87.5 mM | (63) |
| Membrane potential | $V_{pm}$ | −90 mV | (64,65) |
| $K_m$ for extracellular calcium | $K_{Ca,out}$ | 1.38 mM | (63) |
| $K_m$ for intracellular calcium | $K_{Ca,in}$ | 3.59 $\mu$M | (47) |
| $K_m$ for intracellular sodium | $K_{Ca,in}$ | 12.29 mM | (47) |
| | $k_{sat}$ | 0.1 | (63) |
| | $\eta$ | 0.35 | (63) |
| Extracellular [sodium] | $Na_{out}$ | 138 mM | |
| Intracellular [sodium] | $Na_{in}$ | 14.763 mM | (50) |
| PM leakage | Balances PMCA and NCX at baseline $[Ca]_{cyt}$ | | |
| Mitochondria | | | |
| Uniporter $V_{max}$ | $V_{max,uni}$ | 1.875 $\mu$M/s ($[Ca_{mit}]$) | (24) |
| $K_d$ for translocated $Ca^{2+}$ | $K_{uni,\ trans}$ | 19 $\mu$M ($[Ca_{cyt}]$) | (24) |
| $K_d$ for activating $Ca^{2+}$ | $K_{uni,\ act}$ | 0.38 $\mu$M ($[Ca_{cyt}]$) | (24) |
| Activation cooperativity | $n\_a$ | 2.8 | (24) |
| $K_{eq}$ for uniporter conformations | $L$ | 110 | (24) |

(*Continued*)

**TABLE 2. Continued**

| Parameter | Symbol | Value | Source |
|---|---|---|---|
| Offset for $Ca^{2+}$ transport | $\Delta\Psi^*$ | 91 mV | (24) |
| Mitochondrial calcium exchanger | $V_{max,\ mCX}$ | 16.3 nM/s ($[Ca_{mit}]$) | (66) |
| | $K_{mCX,Ca}$ | 3.03 $\mu$M ($[Ca_{mit}]$) | (66) |
| | $K_{mCX,Na}$ | 9.4 mM ($[Na_{cyt}]$) | (66) |
| $IP_3R$ channels (type II) | | | |
| Number of $IP_3Rs$/cell | $n_{IP3R}$ | 14,000 | (14) |
| Maximal flux rate at resting ER-cytosol $Ca^{2+}$ concentration gradient | $V_{IP3R}$ | 0.075 pA | (36) |
| $IP_3R$ model (see Fig. S1) | | modified DeYoung-Keizer | modified Shuai |
| $IP_3$ binding | $k_1$ | 400 $\mu M^{-1}\ s^{-1}$ | 60 $\mu M^{-1} s^{-1}$ |
| | $k_{-1}$ | $6s^{-1}$ | 0.9 $s^{-1}$ |
| $Ca^{2+}$ binding to inhibition site | $k_2$ | 0.2 $\mu M^{-1}\ s^{-1}$ | 0.2 $\mu M^{-1}\ s^{-1}$ |
| | $k_{-2}$ | 0.049 $s^{-1}$ | 3.2 $s^{-1}$ |
| $IP_3$ binding | $k_3$ | 400 $\mu M^{-1}\ s^{-1}$ | 5 $\mu M^{-1}\ s^{-1}$ |
| | $k_{-3}$ | 391.28 $s^{-1}$ | 4 $s^{-1}$ |
| $Ca^{2+}$ binding to inhibitory site | $k_4$ | 0.2 $\mu M^{-1}\ s^{-1}$ | 0.5 $s^{-1}$ |
| | $k_{-4}$ | 0.000758 $s^{-1}$ | 0.036 $\mu M^{-1}\ s^{-1}$ |
| $Ca^{2+}$ binding to activation site | $k_5$ | 20 $\mu M^{-1}\ s^{-1}$ | 150 $\mu M^{-1}\ s^{-1}$ |
| | $k_{-5}$ | 1.268 $s^{-1}$ | 120 $s^{-1}$ |
| conformation change | $k_6$ | 200 $s^{-1}$ | 540 $s^{-1}$ |
| | $k_{-6}$ | 38.2 $s^{-1}$ | 80 $s^{-1}$ |
| $IP_3$ dynamics | | | |
| PLC$\gamma$ | $n_{PLC\gamma}$ | 148,000 ($PLC_{\gamma 2}$) | Membrane associated (17) |
| | | 15,000 ($PLC_{\gamma 1}$) | Membrane associated (17) |
| Resting PLC activity | $V_{PLC,0}$ | 0.4 $\mu$M/s | (4,18) |
| PLC activity after activation | $V_{PLC,max}$ | 0.86–10 $\mu$M/s | (18) |
| PLC time constant | $\tau_{PLC}$ | 90 s | (18) |
| $K_d$ for PLC activation by $Ca^{2+}$ | $K_{PLC,\ ca}$ | 1.1 $\mu$M | (18) |
| $IP_3$ degradation | $V_{IP3,\ deg}$ | 1.333 $s^{-1}$ | (18) |
| **REACTIONS** | | | |
| ER buffer-calreticulin | | | |
| *Site C* | | | |
| Dissociation | $K_{CrtC}$ | 2 mM | (33) |
| Capacity | $s_{CrtC}$ | 20 mol Ca/mol | (33,34) |
| Forward rate | $k_{CrtC+}$ | $1 \times 10^5\ M^{-1}\ s^{-1}$ | Estimate based on ''slower version'' of calmodulin |
| *Site P* | | | |
| Dissociation | $K_{CrtP}$ | 10 $\mu$M | (33) |
| Capacity | $s_{CrtP}$ | 1 mol Ca/mol B | (34) |
| Forward rate | $k_{CrtP+}$ | $1 \times 10^8\ M^{-1}\ s^{-1}$ | Estimate based on ''faster version'' of calmodulin |
| Cytosolic buffer-calmodulin | | | |
| *Site N* | | | |
| Dissociation | $K_{CaMN}$ | 2.6 $\mu$M | (32) |
| Capacity | $s_{CaMN}$ | 2 mol Ca/mol | (32) |
| Forward rate | $k_{CaMN+}$ | 1.6 x $10^8\ M^{-1}\ s^{-1}$ | (32) |
| *Site C* | | | |
| Dissociation | $K_{CaMC}$ | 1 $\mu$M | (32) |
| Capacity | $s_{CaMC}$ | 2 mol Ca/mol | (32) |
| Forward rate | $k_{CaMC+}$ | $2.3 \times 10^6\ M^{-1}\ s^{-1}$ | (32) |
| Mitochondrial buffer | | | |
| Dissociation | $K_{mit\_buffer}$ | 5 $\mu$M | (35) |
| Forward rate | $k_{mit}$ | $10^8\ M^{-1}\ s^{-1}$ | (35) |
| $IP_3$ $IP_3R$ reaction | | | |
| Forward rate | $k_{IP3R\text{-}IP3}$ | $400 \times 10^6\ M^{-1}\ s^{-1}$ | (21) |
| Dissociation | $K_{IP3R\text{-}IP3}$ | 2 $\mu$M | (21) |
| ***Complex mitochondrial model*** | | | (24) all |
| Resp. chain complex concentration | $\rho_{res}$ | 0.4 nmol/mg protein | |
| Equilibrium constant | $K_{res}$ | $1.35 \times 10^{18}$ | |
| Mitochondrial NADH | $NADH_m$ | 0.05 mM | |
| Mitochondrial $NAD^+$ | $NAD^+_m$ | 9.95 mM | |
| $pH_i$-$pH_m$ | $\Delta pH$ | −0.4 | |

**TABLE 2. Continued**

| Parameter | Symbol | Value | Source |
|---|---|---|---|
| | $r_a$ | $6.394 \times 10^{-10}$/s | |
| | $r_b$ | $1.762 \times 10^{-13}$/s | |
| | $r_1$ | $2.077 \times 10^{-18}$ | |
| | $r_3$ | $1.059 \times 10^{-26}$ | |
| | $\Delta\Psi_B$ | 50 mV | |
| Voltage factor | $g$ | 0.85 | |
| Fraction effective $\Delta\Psi$ | $f$ | 0.5 | |
| $J_{H,\ leak}$ conductance | $g_H$ | 0.2 nmol $min^{-1}$ $mV^{-1}$ mg $protein^{-1}$ | |
| | $p_a$ | $1.656 \times 10^{-5}$/s | |
| | $p_b$ | $3.373 \times 10^{-7}$/s | |
| | $p_{c1}$ | $9.651 \times 10^{-14}$/s | |
| | $p_{c2}$ | $4.845 \times 10^{-19}$/s | |
| | $p_1$ | $1.346 \times 10^{-8}$/s | |
| | $p_2$ | $7.739x10^{-7}$/s | |
| | $p_3$ | $6.65 \times 10^{-15}$/s | |
| inner membrane capacitance | $C_{mito}$ | $1.45 \times 10^{-3}$ nmol $mV^{-1}$.mg $protein^{-1}$ | |
| $H^+$ ATPase concentration | $\rho_F$ | 0.7 nmol mg $protein^{-1}$ | |
| Equilibrium constant | $K_{F1}$ | $1.71 \times 10^6$ mM | |
| Mitochondrial $ATP^{4-}$ | $ATP^{4-}{}_m$ | 0.05 $ATP_m$ | |
| Mitochondrial $ADP^{3-}$ | $ADP^{3-}{}_m$ | $0.45 \times 0.8 \times ADP_m$ | |
| Cytosolic $ATP^{4-}$ | $ATP^{4-}{}_i$ | 0.05 $ATP_i$ | |
| Cytosolic $ADP^{3-}$ | $ADP^{3-}{}_i$ | 0.45 $ADP_i$ | |

nearby cytoplasm and mitochondria were tracked over time (10 ms, where the typical open time for $IP_3$Rs is ~5 ms). The similarity of the results from the two approaches is apparent in Fig. 6 *D*, where colored lines indicate the individual mitochondrial increases in uniporter transport. In both sets of simulations, only the three mitochondria closest to the calcium release sites (Fig. 6 *D*, *left*, *y* axis) take up calcium. There was very little change in free internal calcium concentrations (<100 nM) in these three mitochondria (Fig. 6 *D*, *right*, *y* axis).

Collectively, these data point to several important conclusions: First, mitochondrial transport is not uniformly activated during a short, localized calcium response. Second, the high buffering capabilities of mitochondria render the average calcium concentration in the mitochondrial matrix relatively insensitive to very transient events. However, we expect that prolonged localized calcium release could under similar conditions lead to significant differences in calcium level between individual mitochondria (see also (25,26)). Finally, although both spatial simulation approaches give similar results, the random diffusive behavior of individual calcium ions and range of variability for the response, can be explored only in the stochastic model.

## Proximity of $IP_3$Rs to plasma membrane and mitochondria membranes differentially influences their open probability

Both the stochastic and reaction-diffusion geometric models (above) show that cellular architecture can set the stage for local and dynamic heterogeneities in ctosolic calcium concentration. Therefore, we next evaluated how constricted cytoplasmic spaces and the proximity to membranes with different transporter species might influence $IP_3$R open probability and resulting changes in local calcium concentration. We used a very simplified approach, representing the channel neighborhood as volume fractions of individual organelles in a 1D PDE reaction-diffusion model with spherical symmetry. Release from the channel was modeled using the equations

$$\begin{aligned} \frac{\partial C_{\mathrm{Ca},i}}{\partial t} &= D^*_{\mathrm{Ca}i}, \nabla^2 C_{\mathrm{Ca},i} + \sum \Phi_{ik} + \sum_j J_{ij}/(\alpha_i V) \\ \frac{\partial B_{ik}}{\partial t} &= D^*_{ik} \nabla^2 B_{ik} + \Phi_{ik} \end{aligned} \quad . \quad (1)$$

Here, $C_{\mathrm{Ca},i}$ represents calcium concentration within a given compartment $i$ (cytosol, ER, and mitochondria), $B_{ik}$ is the concentration of free buffer $k$ (no calcium bound) within a given compartment $i$ (cytosol, ER, and mitochondria), $D^*$ is the apparent diffusion coefficient (based on results shown in Fig. 3), $\Phi_{ik}$ represents reactions between calcium and the buffers, $J_{ij}$ represents fluxes (in mol/s) from compartment $j$ (cytosol, ER, mitochondria, and extracellular space (ECS)) to compartment $i$, $\alpha_i$ represents the volume fraction occupied by a given organelle, and $V$ represents the volume of a particular spherical shell. All variables are functions of $r$ (radial distance) and, with the exception of $\alpha_i$ and $V$, functions of time. For details, see Appendix.

Fig. 7, *A–H*, shows the effect of cytosol volume in the neighborhood of $IP_3$ receptors on calcium concentration in the cytosol (*A* and *E*) and ER (*B* and *F*), and calmodulin (*C* and *G*) and calreticulin saturation (*D* and *H*) during $IP_3$R activity. The plots show that steeper calcium gradients are created in areas where $IP_3$ receptors face narrow spaces

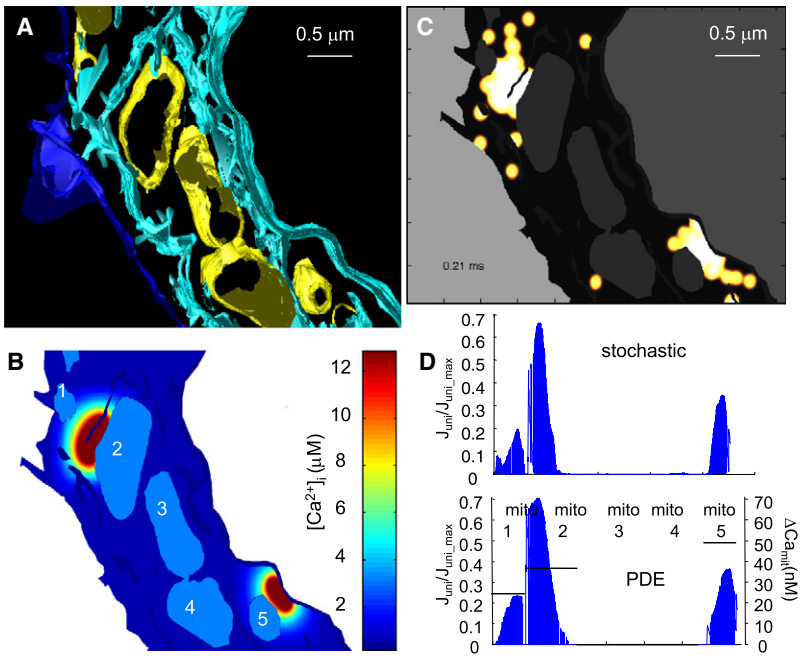


FIGURE 6 Spatial inhomogeneity during $IP_3R$ activity. Local domains of high calcium concentration result in much higher activity of transport mechanisms/buffer saturation in close vicinity to the channels. (*A*) Mitochondria-rich section of the 3D reconstruction. (*B*) Cytosolic calcium concentration after release from two $IP_3R$ clusters with five (*left*) and three (*right*) active $IP_3Rs$. PDE-based approach (model 2) was used. (*C*) The same experiment using the stochastic model. (*D*) Mitochondrial uniporter activity (assuming half-maximum activity at $[Ca^{2+}]_i = 19$ $\mu$M) at various sites of the mitochondrial membrane (at time $t = 4$ ms), expressed as a percentage of the maximal uniporter activity (*left* y *axis*). (*Upper*) Stochastic solution; (*lower*) PDE solution. Also shown in the lower plot is the increase in mitochondrial matrix calcium concentration (*right* y *axis*, also at $t = 4$ ms), with ordinates as numbered areas of mitochondrial membrane.

(*E–H*) confined by neighboring membranes (see also Fig. S2). These narrow spaces can be formed by involutions of the ER itself or by proximity to the plasma membrane or mitochondria. They also show that saturation can occur much faster in constricted spaces.

We further considered the fact that the organelles of each membrane themselves transport calcium at different rates. The ER membrane contains the relatively slow SERCA pumps, the plasma membrane effluxes calcium using plasma membrane calcium ATPase (PMCA) pumps, as well as sodium-calcium exchangers, and the mitochondrial membrane takes up calcium through the efficient uniporter. In Fig. 7, *I* and *J*, we compared local concentrations of calcium (at a distance of 10 and 25 nm) near open channels, located close to either the plasma membrane (*red line*) or mitochondria (*green line*), or far from both organelles. Channels were manually opened at time $t = 0$ and left open for several milliseconds (1 ms shown), on the order of the typical open dwell time of an $IP_3R$ (27,28). Simulations were performed for >1000 channel locations; to meet the ''close'' criterion, the channel had to fall within 75 nm of another membrane. Results show that the levels of local calcium were slightly higher in tight spaces between the ER and the plasma membrane. It is worthy of note that the efficient uptake of calcium by mitochondria translated to the lowest average cytosolic calcium values, despite the narrow spaces between ER and mitochondria. Fig. 7 *J* shows that the local environment also affects the rate of ER emptying: lumenal ER concentrations near channels deplete to a larger extent if the $IP_3Rs$ are near the transport mechanisms operating in plasma membrane or mitochondria.

These differences due to the local environment also have strong implications for feedback regulation of the $IP_3R$. Using the nine-state $IP_3R$ model, we found that under these conditions, channels located close to mitochondria have slightly lower opening probability (15 ± 3%) than channels far from mitochondria (24 ± 6%) (see also Fig. 7, *K* and *L*) resulting in reduced depletion of calcium from the ER.

## DISCUSSION

The problem of using simplified local microdomain geometry in a large-scale calcium model has been approached by others (9). However, due to extensive computational requirements, most models of intracellular signaling do not take complicated intracellular geometries into account. Here, we report several methods for incorporating detailed cellular geometry into mathematical models. These methods are computationally frugal and can be performed on a personal computer or small cluster.

In the simplest approach, we measured the range of distances between cellular membranes and calculated the probability that particles diffusing from one cellular organelle encounter the membrane boundary of another organelle at a given distance (Fig. 2). We also show the possible effect of local calcium microdomains on overall calcium concentration and activity of various transport mechanisms (Fig. S3). These effects could be incorporated into compartmental models for improved spatial representation (see Appendix).

Recently, a hybrid stochastic-deterministic approach to $IP_3R$ channel dynamics has been used to study $IP_3R$-mediated calcium blips (29) and puffs (14). Our reaction-diffusion model incorporates the hybrid approach to 1), explore the effects of fine-scale geometric features, such as the proximity of the ER to mitochondria, on localized channel activity; and 2), provide a validation strategy for stochastic modeling

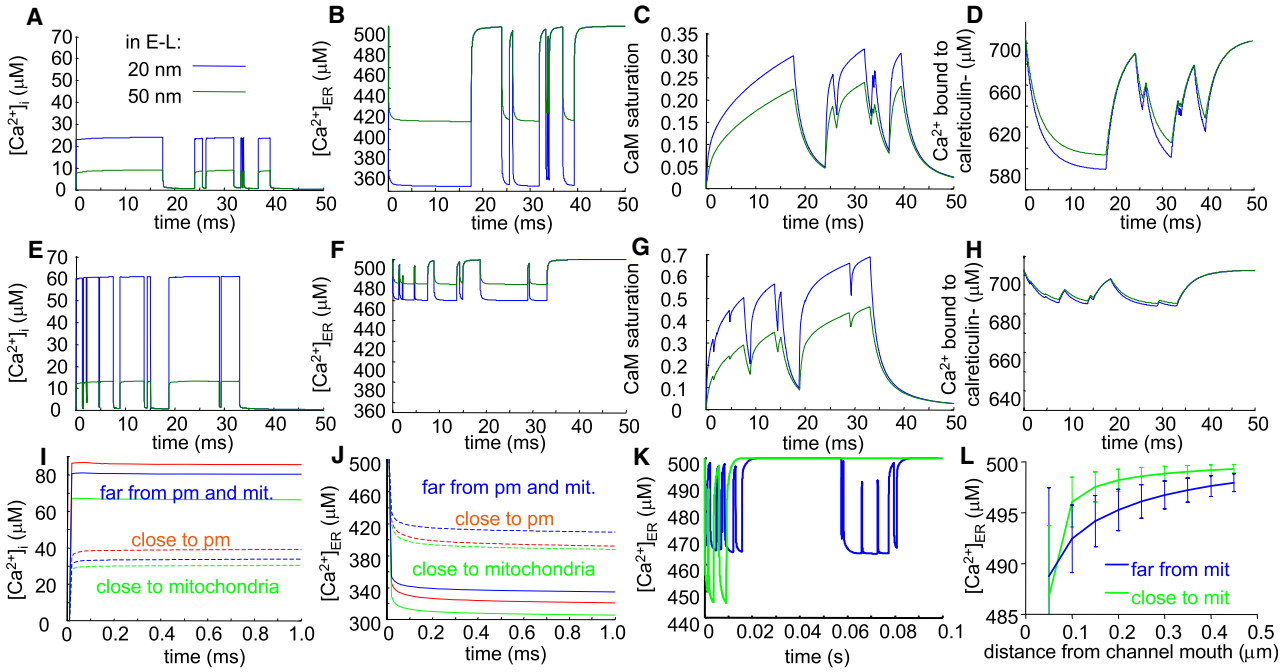


FIGURE 7 Influence of local environment on $IP_3R$ channel activity. Calcium release from a stochastically gated type II $IP_3R$ was modeled using a 1D PDE model and organellar volume fractions (Fig. S2). (A–H) Graphs comparing results for two spatially discrete channels, one in an average location (*A–D*) and one facing a narrow space formed by an ER fold (*E–H*). *A* and *E* compare the nearby changes in cytosolic calcium concentration; *B* and *F* report the nearby ER lumenal calcium concentration; *C* and *G* report calcium binding to calmodulin; and *D* and *H* report calcium binding to calreticulin. Individual traces represent local concentrations at 20 (*blue*) and 50 nm (*green*) from the center of the channel mouth. The resulting increase in cytosolic calcium concentration and calmodulin saturation was much higher in the restricted space. (*I* and *J*) $IP_3R$ locations in the ER membrane were randomly assigned. The volume fraction occupied by nearby organelles was used to define three categories: ''close to mitochondria'', ''close to plasma membrane'', or ''far from either organelle''. The cutoff distance for the close categories was ~75 nm. The $IP_3Rs$ were manually opened at $t = 0$ and left open for 1 ms, and the time courses of calcium concentration in the cytosol (*I*) and the ER (*J*) at 10 nm (*solid lines*) and 25 nm (*dotted lines*) from the center of the channel were plotted. (*K*) Typical ER calcium concentration traces for a channel located at a location far from mitochondria and plasma membrane (*blue*) and a channel close to mitochondria (*green*) 50 nm from the center of the channel mouth. Note that opening of channels close to mitochondria resulted in a more pronounced decrease in ER calcium, but due to lower opening probability, the overall release was reduced. (*L*) Mean (±SE) ER calcium concentration at various distances from the $IP_3R$ channel mouth during 100 ms of $IP_3R$ channel activity.

within the same geometry. PDE approaches are also applied within a simplified geometric context to explore whether localized $IP_3R$ activity leads to calcium gradients in the cytosol and ER lumen. This approach demonstrates that release of calcium from $IP_3Rs$ very near to the plasma membrane transiently generates high local concentrations in the restricted cytosolic volume. In contrast, when $IP_3Rs$ face mitochondria, the efficient uniporter uptake limits the elevation of calcium in the tight space between the two organelles (Fig. 7 *I*). In both cases, there is a steeper loss in ER lumenal calcium near the transporting $IP_3R$ channel (Fig. 7 *J*) than in case where the $IP_3R$ is far from both organelles. We also estimated the implications of tight space upon feedback regulation of the $IP_3$ receptor. Using the nine-state $IP_3R$ model, we found that channels located close to mitochondria would have a slightly lower opening probability than channels far from mitochondria, resulting in reduced depletion of calcium from the ER. This result agrees with the findings of Hajnóczky et al. (30).

Most notably, we report the development of a stochastic spatial model of cellular calcium responses that can be easily adapted to the unique geometries of individual cell types. Large-scale stochastic simulations of calcium dynamics have already been performed by Yi et al. (31), but they lack the details of intracellular architecture. We show how a reconstructed cell slice, based upon an electron tomography tilt series, can easily be traced to serve as the template for spatial stochastic modeling. This technique should also be applicable to more traditional serial ultrathin sections imaged by transmission electron microscopy (TEM) or to stacks of images acquired by confocal microscopy. We demonstrate the capabilities of this model by simulating local $IP_3$ generation and diffusion from a region of the plasma membrane, local activation of $IP_3Rs$ nearest the site of $IP_3$ production, and variations predicted by changes in receptor expression levels. This approach should be particularly powerful for educational purposes, since it permits computer-based visualization of molecular behavior but remains solidly based upon biophysical and mathematical principles. The stochastic approach is also well suited to analysis of experimental data from single-cell calcium measurements, which display considerable variability.

# APPENDIX

## Introduction

Sections in this appendix provide details about the mathematical approaches applied in this work. Both the fully stochastic and hybrid PDE-based reaction-diffusion models (where only the $IP_3R$ handling is stochastic) use the same basic set of parameters (Table 2) that incorporate the cytosol, the endoplasmic reticulum, the plasma membrane, and mitochondria. Compartmental modeling used for parameter estimation is also described.

## 3D stochastic model of $IP_3$ release, diffusion, reversible binding, and degradation

This model is conceived as a fully stochastic reaction-diffusion geometric model. Our program reads bitmap images or their stacks, interprets the bitmap values as belonging to a certain organelle (see the color coding in Fig. 3 *A*), populates the organelles with given species, and handles their diffusion, reactions, and membrane transport mechanisms. Diffusion was modeled using 0.01- to 1-$\mu$s time steps, and the MATLAB *randn* function (normally distributed random number generator):

$$\begin{aligned} d_i &= randn * (2Ddt)^{0.5} \\ d_i &= dx, dy, dz \end{aligned}, \qquad \text{(A1)}$$

where $dt$ is the time step used in the simulation and $d_i$ is the particle's displacement.

In case the molecule left the cytosolic compartment, a new set of random numbers was generated.

To compute the forward reaction occurrence, the diffusive species (calcium or $IP_3$) matrix was replaced with a matrix where each molecule was represented with a ''point-spread function'' concentration matrix:

$$C(r) = \frac{1}{T}\int_0^T \frac{N}{(4\pi Dt)^{d/2}}\exp\left(-\frac{r^2}{4Dt}\right)dt, \qquad \text{(A2)}$$

where $N$ is the number of particles; $r$ is the radial distance from the original position; $D$ is the diffusion coefficient; $T$ is the time step used; and $d$ is the number of dimensions of the system. If time steps were short enough ($<1$ $\mu$s) that most of the concentration was inside one voxel, this recalculation was not necessary and the original (''1 voxel per particle'') matrix was used instead.

The reactions were then considered to occur if $rand < k_{ij}*C_i*C_j*dt$. Care was taken to have the time step $dt$ short enough that $k_{ij}*C_i*C_j*dt << 1$.

Transport mechanisms (used in Movie S2) were modeled so that the binding sites (for SERCA and PMCA pumps and $IP_3R$ regulatory sites) were located in the voxel adjacent to the pump/receptor in a particular membrane. Again, this was recalculated to concentration (in mol/l) in the given voxel.

In the case of Fig. 5, simulations were repeated many times (typically 10–100 cycles). For each cycle, the PLC molecules and $IP_3$ receptors were distributed randomly in the plasma and ER membrane, respectively. In a subset of experiments, the $IP_3Rs$ were clustered (10–100 receptors/cluster). Released $IP_3$ molecules were then allowed to diffuse in the cytosol and bind to the $IP_3Rs$.

## Hybrid model for $IP_3R$ dynamics in the PDE geometric model

We developed a hybrid model combining stochastic $IP_3R$ dynamics and its regulation by released calcium with a deterministic PDE model of calcium diffusion, buffering, and transmembrane transport.

For simplicity, the model was conceived as a spherically symmetrical 1D (radial) PDE model where the neighborhood of the channel was mapped into organelles and intracellular compartments and represented as their volume fraction that varied with radial distance (see Fig. S2). We started with the same equations and parameters as for the compartmental model. The fluxes were adjusted to the spherical symmetry of the model and the diffusion terms were included. The $IP_3R$ current represented the boundary condition (for $r \to 0$). Other fluxes were adjusted in the following manner:

$$J_{ij,r} = J_{ij}\frac{\alpha_{ij,\mathrm{mem},r}}{\alpha_{ij,\mathrm{mem,cell}}}, \qquad \text{(A3)}$$

where $J_{ij,r}$ is the flux from compartment $i$ to compartment $j$ at a distance $r$ from the $IP_3R$ channel mouth; $J_{ij}$ is the flux from compartment $i$ to compartment $j$ in the compartmental model; $\alpha_{ij\ ,\mathrm{mem,r}}$ is the ratio between the size of the membrane and the volume of the spherical shell at distance $r$ from the channel; $\alpha_{ij\ ,\mathrm{mem,cell}}$ is the ratio between the size of the membrane and the volume of the cell.

## Parameter estimation based upon compartmental modeling

Simulations were performed in a MATLAB compartmental model to establish the most probable set of parameters for individual transport mechanisms (Fig. S4). The general approach is described by the equation

$$\begin{aligned} \frac{df_i}{dt} &= \Phi_i + \sum_j J_{ij}/V_i \\ i &= \mathrm{cyt}, \mathrm{ER}, \mathrm{mit}; j = \mathrm{cyt}, \mathrm{ER}, \mathrm{mit}, \mathrm{ECS} \end{aligned}. \qquad \text{(A4)}$$

Here, $S_i$ represents individual species (calcium or free calcium buffers) within a given compartment $i$ (cytosol, ER, mitochondria), $\Phi_i$ the reactions between calcium and the buffers, $J_{ij}$ the fluxes from compartment $j$ (cytosol, ER, mitochondria, ECS) to compartment $i$, and $V_i$, the volume occupied by a given organelle.

## Model details

### *Buffering reactions*

Buffers in the ER and cytosol were represented by calreticulin and calmodulin, respectively. Each of these protein buffers has two types of binding sites with very different calcium-binding affinities (32–34), which are included in our models. In the case of calreticulin, these sites are usually referred to as ''C'' and ''P'', where site C is the larger capacity site, which can bind ~20 mol $Ca^{2+}$/mol protein. Site P, on the other hand, binds only ~1 mol $Ca^{2+}$/mol protein (34). In the model, these sites are represented as $Bc_{\mathrm{er}}$ and $Bp_{\mathrm{er}}$ (unoccupied sites) and $TotBc_{\mathrm{er}}$ and $TotBp_{\mathrm{er}}$ represent the total concentration of the buffering sites. Calmodulin's two binding sites (at the N- and C-termini) are of the same capacity, 2 mol $Ca^{2+}$/mol protein, and again this capacity is reflected in the initial concentrations. Similar to the ER buffers, these are represented as $Bn_{\mathrm{cyt}}$, $Bc_{\mathrm{cyt}}$ and $TotBn_{\mathrm{cyt}}$ and $TotBc_{\mathrm{cyt}}$. For mitochondria, we considered a high-concentration buffer similar to that used by Gerencser et al. (35) ($B_{\mathrm{mit}}$ and $TotB_{\mathrm{mit}}$).

Our mass-action kinetics reaction scheme is as follows:

$$\begin{aligned} \Phi_{\mathrm{Cer\_buffer}} &= -k_{\mathrm{CrtC}+}(C_{\mathrm{er}} \times Bc_{\mathrm{er}}) + k_{\mathrm{CrtC}-}(TotBc_{\mathrm{er}} - Bc_{\mathrm{er}}) \\ &\quad -k_{\mathrm{CrtP}+}(C_{\mathrm{er}} \times Bp_{\mathrm{er}}) + k_{\mathrm{CrtP}-}(TotBp_{\mathrm{er}} - Bp_{\mathrm{er}}) \\ &= \Phi_{\mathrm{Bcer}} + \Phi_{\mathrm{Bper}}. \\ \Phi_{\mathrm{Ccyt\_buffer}} &= -k_{\mathrm{CaMC}+}(C_{\mathrm{cyt}} \times Bc_{\mathrm{cyt}}) + k_{\mathrm{CaMC}-}(TotBc_{\mathrm{cyt}} - Bc_{\mathrm{cyt}}) \\ &\quad -k_{\mathrm{CaMN}+}(C_{\mathrm{cyt}} \times Bn_{\mathrm{cyt}}) + k_{\mathrm{CaMN}-}(TotBn_{\mathrm{cyt}} - Bn_{\mathrm{cyt}}) \\ &= \Phi_{\mathrm{Bccyt}} + \Phi_{\mathrm{Bncyt}}. \\ \Phi_{\mathrm{Cmit\_buffer}} &= -k_{\mathrm{mit}+}(C_{\mathrm{mit}} \times B_{\mathrm{mit}}) + k_{\mathrm{mit}-}(TotB_{\mathrm{mit}} - B_{\mathrm{mit}}) \\ &= \Phi_{\mathrm{Bmit}}. \end{aligned} \qquad \text{(A5)}$$

where $C_{er}$, $B_{Cer}$, $B_{Per}$, $C_{cyt}$, $B_{Ccyt}$, $B_{Ncyt}$, $C_{mit}$, and $B_{mit}$ represent the concentrations of free calcium and unbound buffers in the ER, cytosol, and mitochondria, respectively.

### Membrane transport

The flux terms for calcium comprise the flux across the ER membrane, $J_{Ca,ER\_membrane}$; the flux across the plasma membrane, $J_{Ca,plasma\_membrane}$; and the flux across the mitochondrial membrane $J_{Ca,mitochondrial\_membrane}$. The flux across the ER membrane is represented by the SERCA pumps, the ER leak, and the $IP_3$Rs. Plasma membrane fluxes include the plasma membrane leak, the PMCA, and the sodium-calcium exchanger (NCX). Calcium fluxes across the mitochondrial membrane are represented by the uniporter current and the sodium-independent calcium exchanger (mCX).

$$\begin{aligned} J_{Ca_{ER\_membrane}} &= J_{ER\to cyt} = -J_{cyt\to ER} = J_{ERleak} \\ &\quad + J_{IP3R} - J_{SERCA} \\ J_{Ca_{plasma\_membrane}} &= J_{ECS\to cyt} = -J_{cyt\to ECS} = J_{PMLeak} \\ &\quad - J_{PMCA} - J_{NCX}. \\ J_{Ca_{mitochondrial\_membrane}} &= J_{mit\to cyt} = -J_{cyt\to mit} = J_{mCX} - J_{uni}. \end{aligned} \tag{A6}$$

### $IP_3$ receptor channel flux

The $IP_3$R is represented as

$$J_{IP3R} = \frac{V_{IP3R}}{zF} \times \phi_{IP3R}(t) \times \frac{(Ca_{er} - Ca_{cyt})}{(Ca_{er,0} - Ca_{cyt,0})} \tag{A7}$$

where $V_{IP3R}$ is the maximal $IP_3$R channel flux at resting calcium concentration gradient ER-cytosol (0.075 pA (36)); $Ca_{er}$ and $Ca_{cyt}$ are the ER and cytosolic calcium concentrations, respectively; and $\phi_{IP3R}$ describes the state of the $IP_3$R ($\phi_{IP3R} = 1$ in the open state and $\phi_{IP3R} = 0$ in the closed state), which changes according to the stochastic $IP_3$R model used. Several $IP_3$R models were tested, including the DeYoung-Keizer (21), Fraiman-Dawson (37), simplified Means (14), and the original Smith (18) models, as well as that of Mak et al. (38). We adopted a modified DeYoung-Keizer model (Fig. S1), which gives realistic open and closed times and reflects fast channel kinetics. The kinetic parameters were constrained to reflect the high affinity of $IP_3$R type for $IP_3$ (22,39,40). This nine-state approach was also recently used by Shuai et al. (23).

### $IP_3$ dynamics

$IP_3$ dynamics was simulated in a manner similar to that of Smith et al. (18):

$$\begin{aligned} dIP_3/dt &= \left(V_{PLC,0} + (V_{PLC,max} - V_{PLC,0})\left(1 - e^{-(t-t_0)/\tau_{PLC}}\right)\right) \\ &\quad \times \frac{Ca_{cyt}}{K_{PLC,Ca} + Ca_{cyt}} - V_{IP3,deg} IP_3, \end{aligned} \tag{A8}$$

where $t_0$ is the time of activation, $V_{PLC,0}$ and $V_{PLC,max}$ represent the resting and maximal PLC activity, respectively, $\tau_{PLC}$ is the activation time constant, $V_{IP3,deg}$ the speed of $IP_3$ degradation, and $IP_3$ the $IP_3$ concentration.

## ER membrane fluxes

### SERCA pumps and the leak current

Two SERCA pump isoforms are expressed in RBL cells, SERCA2b and SERCA3, roughly at equal levels (41). SERCA2b has a lower activation threshold and is somewhat slower than SERCA3 (42). For simplicity, we used the representation

$$\begin{aligned} J_{SERCA} &= V_{SERCA2b,max} \frac{Ca_{Cyt}^2}{K_{SERCA2b}^2 + Ca_{Cyt}^2} \\ &\quad + V_{SERCA3,max} \frac{Ca_{Cyt}^2}{K_{SERCA3}^2 + Ca_{Cyt}^2}, \end{aligned} \tag{A9}$$

where $V_{SERCA,max}$ is the maximal SERCA flux and $K_{SERCA}$ is its $K_m$ (for the individual isoforms).

The ER leak of calcium from the ER into the cytosol was constructed in such a manner as to balance both the SERCA and the $IP_3$R calcium current at the experimentally observed baseline concentration of ER calcium. Overall, we employ a linear-function representation of the concentration gradient between the ER lumen and cytosolic calcium for luminal calcium leakage into the cytosol, as follows:

$$J_{ERleak} = V_{ERleak} \times \left(Ca_{er} - Ca_{cyt}\right) \times \phi_{shutoff}(Ca_{er}), \tag{A10}$$

where

$$V_{ERleak} = (J_{SERCA}^{baseline} + J_{IP3R}^{baseline}) \times \left[\frac{1}{Ca_{er} - Ca_{cyt}}\right]_{baseline}, \text{ and}$$

$$\phi_{shutoff}(Ca_{er}) = H(Ca_{er} > K_{ER\_leak\_off}).$$

The "baseline" sub- and superscripts indicate that the terms here are at the initial values used for the respective concentrations and hence are constant. Beecroft (43) observed that ER calcium efflux through the leakage mechanism essentially shuts down when luminal calcium levels drop to ~7% of baseline concentration. We represent this aspect of leakage via the $\phi_{shutoff}$ ($Ca_{er}$) function, which is a Heaviside step function.

### Plasma membrane fluxes

Plasma membrane calcium extrusion mechanisms are represented by PMCA pumps and the NCX. The PMCA current was modeled using the following equations (for parameters, see Table 2):

$$\begin{aligned} J_{PMCA,i} &= V_{PMCA,i} \times f_{1,i} \times Ca_{cyt}^n \Big/ \left(\frac{K_{PMCA,Ca,i}^n}{f_{2,i}} + Ca_{cyt}^n\right) \\ f_{1,i} &= \left(1 + \left(f_{V\_PMCA,CaM,i} - 1\right) \times \frac{CaM}{K_{PMCA,CaM,i} + CaM}\right), \\ f_{2,i} &= \left(1 + \left(f_{K\_PMCA,CaM,i} - 1\right) \times \frac{CaM}{K_{PMCA,CaM,i} + CaM}\right) \end{aligned} \tag{A11}$$

where $J_{PMCA,i}$ is the calcium flux mediated by the individual PMCA isoforms; $V_{PMCA,i}$ the maximum flux mediated by the given PMCA isoform; $f_{1,i}$ the factor describing the increase in PMCA activity maximum due to calmodulin; $f_{2,i}$ the factor describing the decrease in $K_m$ for calcium due to calmodulin; $n$ the Hill coefficient; and $K_{PMCA,CaM,i}$ the $K_d$ for calmodulin binding for isoform $i$; $i = 1,4$ (isoforms 1 and 4).

There are four PMCA isoforms, with PMCA2/3 expressed mainly in the brain. In our model we incorporated the PMCA1 and PMCA4 isoforms, as their presence in mast cells was suggested by the microarray data of Jayapal et al. (44). There is controversy in the literature regarding the kinetic parameters of individual PMCA isoforms. We used the parameters experimentally measured by Elwess et al. (45) (for PMCA4) and Guerini et al. (46) (for PMCA1).

We have also included PMCA activation by calmodulin. Binding of calmodulin both increases PMCA activity and decreases its $K_d$ for calcium (45,46). We incorporated both of these effects in the form of multiplication factors (see Eq. A11).

The NCX current was modeled using the following complex formula (adopted from Shannon et al. (47)):

$$J_{NCX} = \frac{1}{1+\left(\frac{K_{Act}}{Ca_{cyt}}\right)^3} \times V_{NCX} \times \frac{1}{K_{Ca,in}Na_{out}^3\left(1+\left(\frac{Na_{in}}{K_{Na,in}}\right)^3\right) + K_{Na,out}^3 Ca_{cyt}\left(1+\frac{Ca_{cyt}}{K_{Ca,in}}\right) + K_{Ca,out}Na_{in}^3 + Na_{in}^3 Ca_{out} + Na_{out}^3 Ca_{cyt}} \times \frac{1}{1 + k_{sat}e^{(\eta-1)V_{pm}\frac{F}{RT}}} \times \left\{e^{\eta V_{pm}\frac{F}{RT}}Na_{cyt}^3 Ca_{out} - e^{(\eta-1)V_{pm}\frac{F}{RT}}Na_{out}^3 Ca_{cyt}\right\}, \quad \text{(A12)}$$

where $J_{NCX}$ is the calcium flux through NCX, $K_{Act}$ the $K_m$ for intracellular calcium at an allosteric site, $V_{NCX}$ the maximum NCX flux, $K_{Na,out}$ the $K_m$ for extracellular sodium, $K_{Ca,in}$ the $K_m$ for intracellular calcium, $K_{Ca,out}$ the $K_m$ for extracellular calcium, $V$ the membrane potential, $F$ the Faraday constant, $R$ the gas constant, $T$ the temperature, $Na_{in}$ the intracellular sodium concentration, $Na_{out}$ the extracellular sodium concentration, $Ca_{cyt}$ the intracellular (cytosolic) calcium concentration, $Ca_{out}$ the extracellular calcium concentration, $\eta$ the position of the energy barrier controlling voltage dependence of $J_{NCX}$, and $k_{sat}$ the saturation factor of $J_{NCX}$ at very negative potentials.

Due to the lack of kinetic data for the various NCX and NCKX isoforms expressed in RBL cells (48), we used the parameters given by Shannon et al. (47) with the maximum rate adjusted using the constraints mentioned above (49). For simplicity, we considered the sodium concentration and plasma membrane potential to be constant. Extracellular sodium concentration was set to a value roughly corresponding to the typical sodium concentration in the serum, and intracellular concentration was set according to Rumpel et al. (50).

The plasma membrane leakage of calcium into the cytosol from the extracellular space was taken to balance the baseline PMCA + NCX activity.

$$J_{PMleak} = V_{PMCA}^{baseline} + V_{NCX}^{baseline}. \quad \text{(A13)}$$

### *Mitochondrial membrane fluxes*

We slightly modified the original model of Magnus and Keizer (24). This was referred to as the "minimal model", which incorporates not only the main calcium transport mechanisms but also $H^+$ transport, NAD, NADH, ATP, and ADP changes and mitochondrial membrane potential. Parameters were based on an extensive literature search (for review, see Gunter et al. (51)).

The calcium transport mechanisms are described using the following equations (for the mitochondrial uniporter and the calcium exchanger, respectively):

$$J_{uni} = V_{max,uni} \times \frac{\frac{Ca_{cyt}}{K_{uni,trans}}\left(1+\frac{Ca_{cyt}}{K_{uni,trans}}\right)^3}{\left(1+\frac{Ca_{cyt}}{K_{uni,trans}}\right)^4 + \frac{L}{\left(1+\frac{Ca_{cyt}}{K_{uni,act}}\right)^{n\_a}}} \frac{\frac{2F(\Delta\Psi-\Delta\Psi*)}{RT}}{1-\exp\left[\frac{-2F(\Delta\Psi-\Delta\Psi*)}{RT}\right]} \quad \text{(A14)}$$

$$J_{mCX} = V_{max,mCX} \times \frac{Ca_{mit}}{Ca_{mit} + K_{mCX,Ca}} \times \frac{Na_{cyt}^2}{Na_{cyt}^2 + K_{mCX,Na}^2}. \quad \text{(A15)}$$

Here, $V_{max,uni}$ is the maximal current through the uniporter, $K_{uni,trans}$ the $K_m$ for transported calcium; $K_{uni,act}$ the $K_m$ for allosteric activation site, $n\_a$ the Hill coefficient for the allosteric activation site; $\Delta\Psi$ the inner mitochondrial membrane potential; $\Delta\Psi*$ the potential profile within the pore of the uniporter (24); $V_{max,mCX}$ the maximal current carried by the mitochondrial calcium exchanger, and $Ca_{mit}$ the free calcium concentration in mitochondrial matrix space.

To compute the changes in mitochondrial membrane potential, we used the following equations provided by Magnus and Keizer (24). These equations take into account the respiration-driven proton pumps ($J_{H,res}$), the proton-driven mitochondrial ATPase that synthesizes the ATP ($J_{H,F1}$), the adenine nucleotide translocator ($J_{ANT}$) and proton leak over the inner mitochondrial membrane ($J_{H,leak}$):

$$C_{mito}\frac{d\Delta\Psi}{dt} = -(-J_{H,res} + J_{H,F1} + J_{ANT} + J_{H,leak} + 2J_{uni}) \quad \text{(A16)}$$

$$J_{H,res} = 360\rho_{res}\frac{r_a 10^{6\Delta pH}\exp\left(\frac{FA_{res}}{RT}\right) - [r_a + r_b]\exp\left(\frac{g6F\Delta\Psi}{RT}\right)}{\left[1 + r_1\exp\left(\frac{FA_{res}}{RT}\right)\right]\exp\left(\frac{g6F\Delta\Psi_B}{RT}\right) + \left[r_2 + r_3\exp\left(\frac{FA_{res}}{RT}\right)\right]\exp\left(\frac{g6F\Delta\Psi}{RT}\right)} \quad \text{(A17)}$$

$$J_{H,F1} = -180\rho_{F1}\frac{p_a 10^{3\Delta pH}\exp\left(\frac{FA_{F1}}{RT}\right) - [p_a + p_b]\exp\left(\frac{3F\Delta\Psi}{RT}\right)}{\left[1 + p_1\exp\left(\frac{FA_{F1}}{RT}\right)\right]\exp\left(\frac{3F\Delta\Psi_B}{RT}\right) + \left[p_2 + p_3\exp\left(\frac{FA_{F1}}{RT}\right)\right]\exp\left(\frac{3F\Delta\Psi}{RT}\right)} \quad \text{(A18)}$$

$$J_{ANT} = J_{max,ANT}\frac{1 - \frac{ATP_i^{4-}ADP_m^{3-}}{ADP_i^{3-}ATP_m^{4-}}\exp\left(\frac{-F\Delta\Psi}{RT}\right)}{\left[1 + \frac{ATP_i^{4-}}{ADP_i^{3-}}\right]\exp\left(\frac{-fF\Delta\Psi}{RT}\right)\left[1 + \frac{ADP_m^{3-}}{ATP_m^{4-}}\right]} \quad \text{(A19)}$$

$$\frac{d\mathrm{ADP}_m}{dt} = J_{\mathrm{ANT}} - J_{\mathrm{p,F1}}, \tag{A20}$$

where

$$A_{\mathrm{res}} = RT/F\ln\left(\frac{K_{\mathrm{res}}\sqrt{\mathrm{NADH}_m}}{\sqrt{\mathrm{NAD}_m^+}}\right)$$

and

$$A_{\mathrm{F1}} = RT/F\ln\left(\frac{K_{F1}\mathrm{ATP}_m}{\mathrm{ADP}_{\mathrm{m,free}}P_{i,m}}\right). \tag{A21}$$

It should be mentioned that in our simulations, the membrane potential changes had a negligible effect on the overall calcium dynamics and were therefore omitted in the spatial models (only A14 and A15 were used).

For the stochastic simulations, many of the membrane transport mechanisms were simplified: NCX and calmodulin regulation of PMCA were omitted, and the mitochondrial uniporter was modeled using the equation of Villalobos et al. (52):

$$J_{\mathrm{uni}} = V_{\mathrm{max,uni}} \times \frac{Ca_{\mathrm{cyt}}^2}{Ca_{\mathrm{cyt}}^2 + K_{\mathrm{uni,trans}}^2}. \tag{A22}$$

## SUPPORTING MATERIAL

Four figures and six movies are available at http://www.biophysj.org/biophysj/supplemental/S0006-3495(09)00019-8.

We thank Janet Oliver, Jeremy Edwards, and other SpatioTemporal Modeling of Cell Signaling Networks members for valuable discussions. We also gratefully acknowledge Mark Ellisman and John Crum for facilitating electron tomography studies at the National Center for Microscopy and Imaging Research at University of California, San Diego, and the Boulder Laboratory for 3-D Electron Microscopy at the University of Colorado, Boulder, for providing the IMOD software.

This work was supported by grants from the National Institutes of Health (NIH R01 AI051575 to B.S.W. and NIH P20 BM0066283 to establish the University of New Mexico Center for SpatioTemporal Modeling of Cell Signaling Networks.

## REFERENCES

1. Bischoff, S. C. 2007. Role of mast cells in allergic and non-allergic immune responses: comparison of human and murine data. *Nat. Rev. Immunol.* 7:93–104.
2. Stump, R. F., J. M. Oliver, E. J. Cragoe, Jr., and G. G. Deanin. 1987. The control of mediator release from RBL-2H3 cells: roles for $Ca^{2+}$, $Na^+$, and protein kinase C1. *J. Immunol.* 139:881–886.
3. Gilfillan, A. M., and C. Tkaczyk. 2006. Integrated signalling pathways for mast-cell activation. *Nat. Rev. Immunol.* 6:218–230.
4. Smith, A. J., Z. Surviladze, E. A. Gaudet, J. M. Backer, C. A. Mitchell, et al. 2001. p110$\beta$ and p110$\delta$ phosphatidylinositol 3-kinases up-regulate FcεRI-activated $Ca^{2+}$ influx by enhancing inositol 1,4,5-trisphosphate production. *J. Biol. Chem.* 276:17213–17220.
5. Zhang, S. L., Y. Yu, J. Roos, J. A. Kozak, T. J. Deerinck, et al. 2005. STIM1 is a $Ca^{2+}$ sensor that activates CRAC channels and migrates from the $Ca^{2+}$ store to the plasma membrane. *Nature.* 437:902–905.
6. Putney, J. W., Jr. 2007. Recent breakthroughs in the molecular mechanism of capacitative calcium entry (with thoughts on how we got here). *Cell Calcium.* 42:103–110.
7. Feske, S., Y. Gwack, M. Prakriya, S. Srikanth, S. H. Puppel, et al. 2006. A mutation in Orai1 causes immune deficiency by abrogating CRAC channel function. *Nature.* 441:179–185.
8. Schuster, S., M. Marhl, and T. Hofer. 2002. Modelling of simple and complex calcium oscillations. From single-cell responses to intercellular signalling. *Eur. J. Biochem.* 269:1333–1355.
9. Higgins, E. R., M. B. Cannell, and J. Sneyd. 2006. A buffering SERCA pump in models of calcium dynamics. *Biophys. J.* 91:151–163.
10. Slepchenko, B. M., J. C. Schaff, I. Macara, and L. M. Loew. 2003. Quantitative cell biology with the Virtual Cell. *Trends Cell Biol.* 13:570–576.
11. Voeltz, G. K., M. M. Rolls, and T. A. Rapoport. 2002. Structural organization of the endoplasmic reticulum. *EMBO Rep.* 3:944–950.
12. Levine, T., and C. Rabouille. 2005. Endoplasmic reticulum: one continuous network compartmentalized by extrinsic cues. *Curr. Opin. Cell Biol.* 17:362–368.
13. Rizzuto, R., and T. Pozzan. 2006. Microdomains of intracellular $Ca^{2+}$: molecular determinants and functional consequences. *Physiol. Rev.* 86:369–408.
14. Means, S., A. J. Smith, J. Shepherd, J. Shadid, J. Fowler, et al. 2006. Reaction diffusion modeling of calcium dynamics with realistic ER geometry. *Biophys. J.* 91:537–557.
15. Griffiths, G., G. Warren, P. Quinn, O. Mathieu-Costello, and H. Hoppeler. 1984. Density of newly synthesized plasma membrane proteins in intracellular membranes. I. Stereological studies. *J Cell Biol.* 98:2133–2141.
16. Pfeiffer, J. R., J. C. Seagrave, B. H. Davis, G. G. Deanin, and J. M. Oliver. 1985. Membrane and cytoskeletal changes associated with IgE-mediated serotonin release from rat basophilic leukemia cells. *J Cell Biol.* 101:2145–2155.
17. Wilson, B. S., J. R. Pfeiffer, Z. Surviladze, E. A. Gaudet, and J. M. Oliver. 2001. High resolution mapping of mast cell membranes reveals primary and secondary domains of FcεRI and LAT. *J. Cell Biol.* 154:645–658.
18. Smith, G. D., R. J. Lee, J. M. Oliver, and J. Keizer. 1996. Effect of $Ca^{2+}$ influx on intracellular free $Ca^{2+}$ responses in antigen-stimulated RBL-2H3 cells. *Am. J. Physiol.* 270:C939–C952.
19. Wilson, B. S., J. R. Pfeiffer, A. J. Smith, J. M. Oliver, J. A. Oberdorf, et al. 1998. Calcium-dependent clustering of inositol 1,4,5-trisphosphate receptors. *Mol. Biol. Cell.* 9:1465–1478.
20. Tateishi, Y., M. Hattori, T. Nakayama, M. Iwai, H. Bannai, et al. 2005. Cluster formation of inositol 1,4,5-trisphosphate receptor requires its transition to open state. *J. Biol. Chem.* 280:6816–6822.
21. De Young, G. W., and J. Keizer. 1992. A single-pool inositol 1,4,5-trisphosphate-receptor-based model for agonist-stimulated oscillations in $Ca^{2+}$ concentration. *Proc. Natl. Acad. Sci. USA.* 89:9895–9899.
22. Wojcikiewicz, R. J., and S. G. Luo. 1998. Differences among type I, II, and III inositol-1,4,5-trisphosphate receptors in ligand-binding affinity influence the sensitivity of calcium stores to inositol-1,4,5-trisphosphate. *Mol. Pharmacol.* 53:656–662.
23. Shuai, J., J. E. Pearson, J. K. Foskett, D. O. Mak, and I. Parker. 2007. A kinetic model of single and clustered $IP_3$ receptors in the absence of $Ca^{2+}$ feedback. *Biophys. J.* 93:1151–1162.
24. Magnus, G., and J. Keizer. 1997. Minimal model of beta-cell mitochondrial $Ca^{2+}$ handling. *Am. J. Physiol.* 273:C717–C733.
25. Montero, M., M. T. Alonso, E. Carnicero, I. Cuchillo-Ibanez, A. Albillos, et al. 2000. Chromaffin-cell stimulation triggers fast millimolar mitochondrial Ca2+ transients that modulate secretion. *Nat. Cell Biol.* 2:57–61.
26. Park, M. K., M. C. Ashby, G. Erdemli, O. H. Petersen, and A. V. Tepikin. 2001. Perinuclear, perigranular and sub-plasmalemmal mitochondria have distinct functions in the regulation of cellular calcium transport. *EMBO J.* 20:1863–1874.
27. Tu, H., Z. Wang, and I. Bezprozvanny. 2005. Modulation of mammalian inositol 1,4,5-trisphosphate receptor isoforms by calcium: a role of calcium sensor region. *Biophys. J.* 88:1056–1069.
28. Foskett, J. K., C. White, K. H. Cheung, and D. O. Mak. 2007. Inositol trisphosphate receptor $Ca^{2+}$ release channels. *Physiol. Rev.* 87: 593–658.

29. Rudiger, S., J. W. Shuai, W. Huisinga, C. Nagaiah, G. Warnecke, et al. 2007. Hybrid stochastic and deterministic simulations of calcium blips. *Biophys. J.* 93:1847–1857.

30. Hajnoczky, G., R. Hager, and A. P. Thomas. 1999. Mitochondria suppress local feedback activation of inositol 1,4, 5-trisphosphate receptors by $Ca^{2+}$. *J. Biol. Chem.* 274:14157–14162.

31. Yi, Y. B., H. Wang, A. M. Sastry, and C. M. Lastoskie. 2005. Direct stochastic simulation of $Ca^{2+}$ motion in *Xenopus* eggs. *Phys. Rev. E Stat. Nonlin. Soft Matter Phys.* 72:021913.

32. Johnson, J. D., C. Snyder, M. Walsh, and M. Flynn. 1996. Effects of myosin light chain kinase and peptides on $Ca^{2+}$ exchange with the N- and C-terminal $Ca^{2+}$ binding sites of calmodulin. *J. Biol. Chem.* 271:761–767.

33. Baksh, S., and M. Michalak. 1991. Expression of calreticulin in *Escherichia coli* and identification of its $Ca^{2+}$ binding domains. *J. Biol. Chem.* 266:21458–21465.

34. Michalak, M., E. F. Corbett, N. Mesaeli, K. Nakamura, and M. Opas. 1999. Calreticulin: one protein, one gene, many functions. *Biochem. J.* 344:281–292.

35. Gerencser, A. A., and V. Adam-Vizi. 2005. Mitochondrial $Ca^{2+}$ dynamics reveals limited intramitochondrial $Ca^{2+}$ diffusion. *Biophys. J.* 88:698–714.

36. Bezprozvanny, I., and B. E. Ehrlich. 1994. Inositol (1,4,5)-trisphosphate ($InsP_3$)-gated Ca channels from cerebellum: conduction properties for divalent cations and regulation by intraluminal calcium. *J. Gen. Physiol.* 104:821–856.

37. Fraiman, D., and S. P. Dawson. 2004. A model of $IP_3$ receptor with a luminal calcium binding site: stochastic simulations and analysis. *Cell Calcium.* 35:403–413.

38. Mak, D. O., S. M. McBride, N. B. Petrenko, and J. K. Foskett. 2003. Novel regulation of calcium inhibition of the inositol 1,4,5-trisphosphate receptor calcium-release channel. *J. Gen. Physiol.* 122:569–581.

39. Newton, C. L., G. A. Mignery, and T. C. Sudhof. 1994. Co-expression in vertebrate tissues and cell lines of multiple inositol 1,4,5-trisphosphate ($InsP_3$) receptors with distinct affinities for $InsP_3$. *J. Biol. Chem.* 269:28613–28619.

40. Nerou, E. P., A. M. Riley, B. V. Potter, and C. W. Taylor. 2001. Selective recognition of inositol phosphates by subtypes of the inositol trisphosphate receptor. *Biochem. J.* 355:59–69.

41. Wuytack, F., B. Papp, H. Verboomen, L. Raeymaekers, L. Dode, et al. 1994. A sarco/endoplasmic reticulum $Ca^{2+}$-ATPase 3-type $Ca^{2+}$ pump is expressed in platelets, in lymphoid cells, and in mast cells. *J. Biol. Chem.* 269:1410–1416.

42. Lytton, J., M. Westlin, S. E. Burk, G. E. Shull, and D. H. MacLennan. 1992. Functional comparisons between isoforms of the sarcoplasmic or endoplasmic reticulum family of calcium pumps. *J. Biol. Chem.* 267:14483–14489.

43. Beecroft, M. D., and C. W. Taylor. 1998. Luminal $Ca^{2+}$ regulates passive $Ca^{2+}$ efflux from the intracellular stores of hepatocytes. *Biochem. J.* 334:431–435.

44. Jayapal, M., H. K. Tay, R. Reghunathan, L. Zhi, K. K. Chow, et al. 2006. Genome-wide gene expression profiling of human mast cells stimulated by IgE or FcepsilonRI-aggregation reveals a complex network of genes involved in inflammatory responses. *BMC Genomics.* 7:210.

45. Elwess, N. L., A. G. Filoteo, A. Enyedi, and J. T. Penniston. 1997. Plasma membrane $Ca^{2+}$ pump isoforms 2a and 2b are unusually responsive to calmodulin and $Ca^{2+}$. *J. Biol. Chem.* 272:17981–17986.

46. Guerini, D., B. Pan, and E. Carafoli. 2003. Expression, purification, and characterization of isoform 1 of the plasma membrane $Ca^{2+}$ pump: focus on calpain sensitivity. *J. Biol. Chem.* 278:38141–38148.

47. Shannon, T. R., F. Wang, J. Puglisi, C. Weber, and D. M. Bers. 2004. A mathematical treatment of integrated Ca dynamics within the ventricular myocyte. *Biophys. J.* 87:3351–3371.

48. Aneiros, E., S. Philipp, A. Lis, M. Freichel, and A. Cavalie. 2005. Modulation of $Ca^{2+}$ signaling by Na+/Ca2+ exchangers in mast cells. *J. Immunol.* 174:119–130.

49. Chandra, S., C. Fewtrell, P. J. Millard, D. R. Sandison, W. W. Webb, et al. 1994. Imaging of total intracellular calcium and calcium influx and efflux in individual resting and stimulated tumor mast cells using ion microscopy. *J. Biol. Chem.* 269:15186–15194.

50. Rumpel, E., U. Pilatus, A. Mayer, and I. Pecht. 2000. $Na^{+}$-dependent $Ca^{2+}$ transport modulates the secretory response to the Fcepsilon receptor stimulus of mast cells. *Biophys. J.* 79:2975–2986.

51. Gunter, T. E., L. Buntinas, G. Sparagna, R. Eliseev, and K. Gunter. 2000. Mitochondrial calcium transport: mechanisms and functions. *Cell Calcium.* 28:285–296.

52. Villalobos, C., L. Nunez, M. Montero, A. G. Garcia, M. T. Alonso, et al. 2002. Redistribution of $Ca^{2+}$ among cytosol and organella during stimulation of bovine chromaffin cells. *Faseb. J.* 16:343–353.

53. de Bernard, M., A. Cappon, L. Pancotto, P. Ruggiero, J. Rivera, et al. 2005. The Helicobacter pylori VacA cytotoxin activates RBL-2H3 cells by inducing cytosolic calcium oscillations. *Cell. Microbiol.* 7:191–198.

54. Mohr, F. C., and C. Fewtrell. 1987. Depolarization of rat basophilic leukemia cells inhibits calcium uptake and exocytosis. *J. Cell Biol.* 104:783–792.

55. Lin, P., W. J. Fung, and A. M. Gilfillan. 1992. Phosphatidylcholine-specific phospholipase D-derived 1,2-diacylglycerol does not initiate protein kinase C activation in the RBL 2H3 mast-cell line. *Biochem. J.* 287:325–331.

56. Ehring, G. R., H. H. Kerschbaum, C. M. Fanger, C. Eder, H. Rauer, and M. D. Cahalan. 2000. Vanadate induces calcium signaling, $Ca^{2+}$ release-activated $Ca^{2+}$ channel activation, and gene expression in T lymphocytes and RBL-2H3 mast cells via thiol oxidation. *J. Immunol.* 164:679–687.

57. Yu, R., and P. M. Hinkle. 2000. Rapid turnover of calcium in the endoplasmic reticulum during signaling. Studies with cameleon calcium indicators. *J. Biol. Chem.* 275:23648–23653.

58. Csordas, G., M. Madesh, B. Antonsson, and G. Hajnoczky. 2002. tcBid promotes $Ca^{2+}$ signal propagation to the mitochondria: control of Ca(2+) permeation through the outer mitochondrial membrane. *EMBO J.* 21:2198–2206.

59. Xu, Z., C. J. Williams, G. S. Kopf, and R. M. Schultz. 2003. Maturation-associated increase in IP3 receptor type 1: role in conferring increased IP3 sensitivity and $Ca^{2+}$ oscillatory behavior in mouse eggs. *Dev. Biol.* 254:163–171.

60. Luzzi, V., C. E. Sims, J. S. Soughayer, and N. L. Allbritton. 1998. The physiologic concentration of inositol 1,4,5-trisphosphate in the oocytes of Xenopus laevis. *J. Biol. Chem.* 273:28657–28662.

61. Allbritton, N. L., T. Meyer, and L. Stryer. 1992. Range of messenger action of calcium ion and inositol 1,4,5-trisphosphate. *Science.* 258:1812–1815.

62. Luby-Phelps, K., M. Hori, J. M. Phelps, and D. Won. 1995. $Ca^{2+}$-regulated dynamic compartmentalization of calmodulin in living smooth muscle cells. *J. Biol. Chem.* 270:21532–21538.

63. Luo, C. H., and Y. Rudy. 1994. A dynamic model of the cardiac ventricular action potential. I. Simulations of ionic currents and concentration changes. *Circ. Res.* 74:1071–1096.

64. Sagi-Eisenberg, R., and I. Pecht. 1984. Resolution of cellular compartments involved in membrane potential changes accompanying IgE-mediated degranulation of rat basophilic leukemia cells. *EMBO J.* 3:497–500.

65. Kanner, B. I., and H. Metzger. 1983. Crosslinking of the receptors for immunoglobulin E depolarizes the plasma membrane of rat basophilic leukemia cells. *Proc. Natl. Acad. Sci. USA.* 80:5744–5748.

66. Wingrove, D. E., and T. E. Gunter. 1986. Kinetics of mitochondrial calcium transport. II. A kinetic description of the sodium-dependent calcium efflux mechanism of liver mitochondria and inhibition by ruthenium red and by tetraphenylphosphonium. *J. Biol. Chem.* 261:15166–15171.